JGR Oceans

RESEARCH ARTICLE
10.1029/2020JC016749

Special Section:
Years of the Maritime Continent

Near-Inertial Wave Propagation in the Wake of Super Typhoon Mangkhut: Measurements From a Profiling Float Array

T. M. Shaun Johnston[1], Shuguang Wang[2], Chia-Ying Lee[3], James N. Moum[4], Daniel L. Rudnick[1], and Adam Sobel[2,3]

[1]Scripps Institution of Oceanography, University of California, San Diego, CA, USA, [2]Department of Applied Physics and Applied Mathematics, Columbia University, New York, NY, USA, [3]Lamont Doherty Earth Observatory, Columbia University, New York, NY, USA, [4]College of Earth, Ocean, and Atmospheric Sciences, Oregon State University, Corvallis, OR, USA

Key Points:

- Mean flow over isopycnals displaced by near-inertial internal waves (NIWs) generates secondary, vertically-propagating, and shorter NIWs
- The tropical cyclone (TC) wake's vorticity and shear alter NIW frequency and wavelength, allowing vertical propagation
- Downward NIW energy flux is ~6% of this TC's energy flux from wind forcing to mixed layer near-inertial kinetic energy

Supporting Information:

- Supporting Information S1

Correspondence to:
T. M. S. Johnston,
shaunj@ucsd.edu

Citation:
Johnston, T. M. S., Wang, S., Lee, C.-Y., Moum, J. N., Rudnick, D. L., & Sobel, A. (2021). Near-inertial wave propagation in the wake of Super Typhoon Mangkhut: Measurements from a profiling float array. *Journal of Geophysical Research: Oceans*, *126*, e2020JC016749. https://doi.org/10.1029/2020JC016749

Received 28 AUG 2020
Accepted 5 DEC 2020

Abstract Near-inertial internal waves (NIWs) are generated by inertially-rotating winds under tropical cyclones (TC). Since NIWs are mostly horizontal, their vertical propagation out of the mixed layer is slow. However, mesoscale vorticity and shear increase vertical group speed by increasing near-inertial frequency and horizontal wavenumber. To assess NIW propagation, a profiling float array under Super Typhoon Mangkhut in September 2018 made broad and persistent measurements in space and time of density in the upper 200 m and depth-mean velocity. The TC wake was a region of positive vorticity on its southern side, displayed elevated shear, and thereby enhanced downward propagation of NIWs. The vertical energy flux is estimated as 0.04–0.11 W m^{-2}, which is about 1%–4% (3%–8%) of the mean total (near-inertial) wind work of 3.0 (1.3) W m^{-2} calculated from a high-resolution TC model. Considerable uncertainties arise in the (a) estimated group speed based on wavelength, shear, and frequency and (b) energy density based on depth-varying density and the NIW polarization relations, which are sensitive to frequency. Following the TC's passage, NIWs propagated southward and horizontal wavelengths decreased from 1,000 to 500 km, as time progressed. Also, we identify an interfacial wave at the mixed layer base, which displaces isopycnals vertically. The following process is suggested. As the North Equatorial Current flows over these displacements, which act as topographic obstacles, secondary NIWs propagate up-/downward into the mixed layer/thermocline. These waves are 180° out of phase in the mixed layer and thermocline, which can enhance shear at the mixed layer base.

Plain Language Summary Winds in tropical cyclones (TC) generate near-inertial internal waves (NIWs), which propagate slowly into the ocean's interior. The restoring forces on NIWs are a combination of gravity and Coriolis resulting in slow downward energy propagation into the interior, where breaking NIWs are significant contributors to mixing. We describe three mechanisms (two known, one new), that enhance vertical propagation. The well-known key to downward propagation is the reduction of the horizontal wavelength, which occurs due to (a) rotation of mesoscale eddies and (b) their vertical current shear. A new result is that the TC wake aids downward propagation because it exhibits these two mesoscale properties itself. The third mechanism is new and arises from a NIW found between the mixed layer and ocean interior. This NIW alternately augments and opposes the North Equatorial Current, which leads to flow convergence and vertical excursions of the mixed layer base at a near-inertial frequency, which, in turn, produces both up- and downward propagating NIWs. These measurements were made from profiling floats, which only measured temperature and salinity, and are identical to those widely used in the Argo program, although their mission profile was different.

1. Introduction

At a given point on the right hand side of tropical cyclones (TC), winds rotate in the clockwise direction near the Coriolis frequency (f) and generate near-inertial internal waves (NIWs; Price, 1981). Super Typhoon Mangkhut moved westward across the western North Pacific in September 2018. Ahead of this TC, we deployed an array of profiling floats, which measured NIW generation under the TC (Johnston et al., 2020). Since NIWs have a flat aspect ratio, it limits their vertical propagation and the extraction of

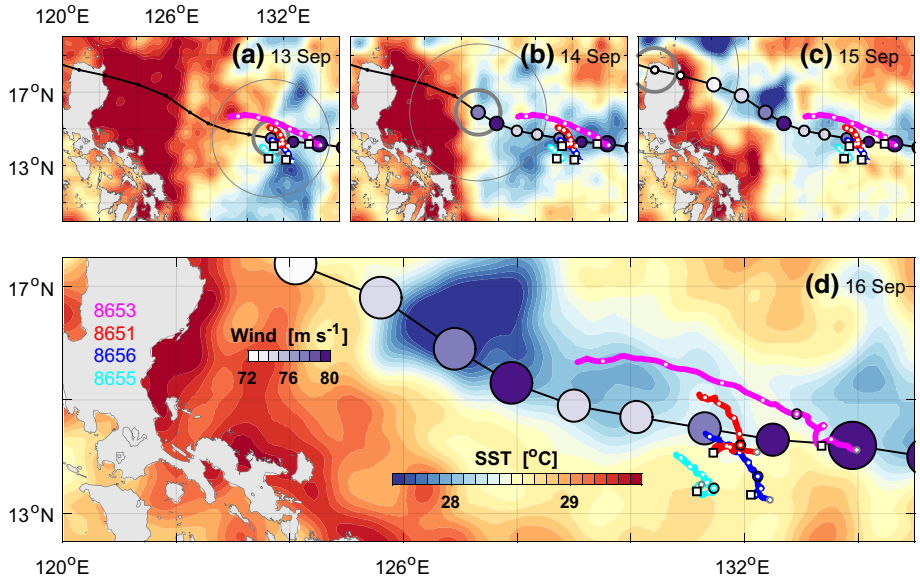

Figure 1. The generally westward progression across the western Pacific of the floats and Super Typhoon Mangkhut are shown. Positions of the TC are shown at 6-h intervals (purple circles) ending at 0000 UTC on (a) September 13, (b) September 14, and (c) September 15, 2018. Daily mean SST shows the TC cold wake. The radii of 18/33 m s^{-1} winds (tropical storm/category-1 TC) are plotted as light/dark gray circles at 0000 UTC. Circle color/size indicates the speed/radius of maximum winds. Float trajectories are thick, colored lines. Float positions are noted at the closest approach of the TC near 0000 UTC on September 13, 2018 (squares), and every 2 days from September 10–25 (white dots). (d) On September 16 float positions are shown (black circles) with starting positions on September 10 (gray circles). SST, sea surface temperature; TC, tropical cyclone.

near-inertial (NI) energy from the mixed layer (Alford et al., 2016). Here, we investigate the vertical and horizontal propagation of NIWs using the float array in the TC wake (Pallàs-Sanz et al., 2016). The main goal is to examine three processes, that enhance vertical propagation. These are: (a) mesoscale vorticity reduces the effective planetary vorticity making the waves more superinertial (Kunze, 1985); (b) vertical shear of horizontal mesoscale currents increases NIW vertical propagation by altering the effective stratification, modifying the dispersion relation, and decreasing their horizontal wavelengths (Kunze, 1985); and (c) secondary short-wavelength NIWs are generated by an interfacial wave in the transition layer, the interface between the mixed layer and ocean interior (Johnston & Rudnick, 2009). Since the TC wake itself is a region of cyclonic vorticity on its equatorward side and displays enhanced shear, it can enhance downward propagation of NIWs like any other mesoscale feature.

NIW vertical propagation speed (i.e., the group speed, c_{gz}), is increased via reduction of the horizontal wavelength (λ_h) and/or increase in the frequency (ω) above f. Initially, λ_h is set by the scale of the atmospheric forcing, which is often >1,000 km for mid-latitude storms, but can be as small as 500 km for TCs, which are more compact (Figure 1; Pallàs-Sanz et al., 2016). Since f varies meridionally with a slope of β, the storm-generated NIWs dephase as they rotate mainly in the horizontal and experience different f at different latitudes. The flow becomes divergent, produces vertical velocity, and allows vertical propagation (D'Asaro et al., 1995). In 21 days (Δt) after the mid-latitude storm described by D'Asaro et al. (1995), kinetic energy (E_k) in the mixed layer was reduced to 10% of its maximum by NIW propagation into the interior. The energy decays exponentially as $\exp(-\Delta t/\tau_e)$, where the decay scale is: $\tau_e = 11$ days. More rapid downward propagation of a single NIW group was noted at a low-latitude mesoscale front (Johnston et al., 2016), where β, relative vorticity, and shear were greater. A field of mesoscale eddies can also dephase the initially large-scale horizontal NI motions (Young & Ben Jelloul, 1997). Background cyclonic vorticity increases the effective f and background shear alters the dispersion relation and c_{gz} (Kunze, 1985; Pallàs-Sanz et al., 2016). Since our measurements are at low latitude compared to studies of mid-latitude storms (D'Asaro et al., 1995) and TCs in the Gulf of Mexico (Pallàs-Sanz et al., 2016), (a) β is larger and (b) horizontal and vertical current shear are elevated in the North Equatorial Current (NEC; Schönau & Rudnick, 2015). These factors increase c_{gz}.

TCs produce vertical energy fluxes of $F_z \sim 0.01$ W m^{-2}, an order of magnitude larger than typical mid-latitude storms (Pallàs-Sanz et al., 2016, and references therein). Energy flux measurements from TCs have typically been made at higher latitudes, but more rapid vertical propagation seems likely at lower latitudes. Furthermore, NIW amplitudes under TCs increase, as latitude decreases (Chang & Anthes, 1978).

This paper aims to calculate the vertical energy flux in the NIWs and the fraction of wind power input to the mixed layer carried away by the NIWs. The paper is organized as follows. Processes reducing the wavelength and thereby enhancing vertical propagation are described. Since the floats measure depth-dependent temperature and salinity, but not velocity, several steps and assumptions are needed to obtain energy flux. Data are described in Section 2. Section 3 describes the wind power input to the mixed layer in a high-resolution model, since we have no local measurements of wind speed. Section 4 explains how NI motions are band-passed to obtain potential energy. Using the polarization relations with depth-dependent density, Section 5 estimates depth-dependent NI velocity and kinetic energy. Next, we examine three processes enhancing vertical energy propagation in the TC wake. Section 6 describes known effects of background vorticity and shear on vertical propagation of NIWs using observed values from the TC wake. Section 7 characterizes an interfacial wave between the thermocline and mixed layer generating down- and upward propagating NIWs. Using both the broad spatial and persistent temporal coverage of the array, we assess the evolution of the horizontal wavenumber (direction and magnitude) of the NIWs with directional harmonic fits in Section 8. The sensitivity of the directional harmonic fits is examined in the supplementary material. Lastly, Section 9 summarizes our observations of NIW propagation in the TC wake. Table 1 provides a summary of variables and abbreviations.

2. Data

The winds and track of Super Typhoon Mangkhut are from the Joint Typhoon Warning Center (Chu et al., 2002). A super typhoon has maximum winds above 67 m s^{-1} in 1-min means, while a typhoon has maximum winds from 33 to 66 m s^{-1}. Mangkhut's winds reached 80 m s^{-1}, when it encountered the floats near 0000 UTC on September 13, 2018. Its non-dimensional translation speed was $s/(2fr) = 2$, where its translation speed is $s = 6$ m s^{-1}, $f = 2\pi/T_i$ where the inertial period is $T_i \sim 2$ days at 14.4°N, and its radius of maximum winds is $r \sim 35$ km (Figure 1). Considerable generation of NIWs is expected for $s/(2fr) > 1$ (D'Asaro et al., 2014). We deployed a SOLO-II float at each of 11, 12, and 13°N near 134.5°W on August 23, 2018 and then again on August 26, after which some of them fortuitously encountered Mangkhut. Two more floats were intentionally placed in advance of the TC on September 8. We describe measurements from the 4 closest floats to Mangkhut.

SOLO-II floats are autonomous, Lagrangian platforms designed and built by the Instrument Development Group at Scripps and are used in the Argo program (R. E. Davis et al., 2001). Our floats profiled more rapidly. A full cycle from the surface to 200 m and back to the surface takes about 38 min at a vertical profiling speed of 0.2 m s^{-1}. They measure temperature (T) and salinity (S), from which potential density (σ_θ) is calculated before, during, and after the TC (Figure 2). Inertial motions are sampled well by the profiling floats. On each dive cycle, a float obtains latitude and longitude from the Global Positioning System, descends, reaches a target depth, records data at 1 Hz during the ascent, obtains a final position, and transmits data via Iridium satellite. From the difference between final and initial positions, a depth-mean velocity over the profiling range is calculated: $\mathbf{u_m}$. The velocity at the surface ($\mathbf{u_s}$) is obtained by differencing positions during the surface interval of about 5 min. This measurement is made over a shorter duration and can be affected by surface waves.

A sea surface temperature (SST) product from the Group for High-Resolution SST uses optimal interpolation to combine numerous datasets (Donlon et al., 2007). SST shows the extent of the TC's cold wake over a wider area than was covered by the floats. The 2 northern floats (8653 and 8651- pink and red lines denote these floats in all figures) experienced the largest NIWs and passed under the eye or within a few kilometers of it resulting in considerable changes in σ_θ and stratification, which is represented by the buoyancy frequency squared: $N^2 = -g\partial_z\sigma_\theta/\rho$, where the in situ density is ρ, the gravitational acceleration is g and the vertical coordinate is z with positive upwards (Figures 2–3). The 2 southern floats (8656 and 8655- dark and light blue lines in all figures) were within several kilometers of the radius of 33 m s^{-1} winds, where measured NIWs were about a factor of 2 weaker than at the northern floats.

Table 1
Glossary

Variable	Definition	Units
NI	Near-inertial	–
NIW	Near-inertial internal wave	–
TC	Tropical cyclone	–
NEC	North Equatorial Current	–
WED	Wavelet energy density	Various
T	Time	Various
F	Coriolis frequency	s^{-1}
$T_i = 2\pi/f$	Inertial period	s
ω	Radial frequency	s^{-1}
$\boldsymbol{x} = (x, y, z)$	Position (positive east-, north-, upward)	Various
$\boldsymbol{k} = (k, l, m)$	Wavenumber (positive east-, north-, upward)	m^{-1}
$\lambda_h = 2\pi/(k, l)$	Horizontal wavelength	m
$\lambda_v = 2\pi/m$	Vertical wavelength	m
c_{gz}	Vertical group speed	m day^{-1}
SST	Sea surface temperature	°C
$T(z, t)$	Temperature	°C
$S(z, t)$	Salinity	psu
$\sigma_\theta(z, t)$	Potential density	kg m^{-3}
$N(z, t)$	Buoyancy frequency	s^{-1}
$\sigma_\theta^{'}(z, t)$	NI bandpassed σ_θ	kg m^{-3}
$A^2\sigma_\theta^{'2}(z,t)$	NI E_p	J m^{-3}
S	TC translation speed	m s^{-1}
$\boldsymbol{U}(t) = (U, V)$	Mean mixed layer velocity (eastward, northward)	m s^{-1}
$\boldsymbol{u_s}(t) = (u_s, v_s)$	Surface velocity (eastward, northward)	m s^{-1}
$\boldsymbol{u_m}(t) = (u_m, v_m)$	Depth-mean velocity (eastward, northward)	m s^{-1}
$\boldsymbol{u_\sigma^{'}}(z, t)$	Depth-varying NI velocity from NI σ_θ'	m s^{-1}
ζ/f	Normalized relative vorticity	–
E_k	Kinetic energy density	J m^{-3}
E_p	Potential energy density	J m^{-3}
$E = E_k + E_p$	Total energy density	J m^{-3}
$R_\omega = E_k/E_p$	Kinetic to potential energy ratio	–
$E_{km}(t), E_m(t)$	E_k, E from $\mathbf{u_m}$	J m^{-3}
$E_{k\sigma}(z, t), E_\sigma(z, t)$	NI E_k, E from NI $\mathbf{u}_\sigma'$	J m^{-3}
$F_z = c_{gz}E$	Vertical energy flux	W m^{-2}
$F_{zm}(t), F_{z\sigma}(z, t)$	NI F_z from NI $\mathbf{u}_m'$, $\mathbf{u}_\sigma'$	W m^{-2}
$\boldsymbol{\tau} = (\tau_x, \tau_y)$	Wind stress (eastward, northward)	Pa
$P = \boldsymbol{U} \cdot \boldsymbol{\tau}$	Energy flux from wind to mixed layer E_k	W m^{-2}
P'	P to mixed layer NI E_k	W m^{-2}
$\theta = tan^{-1}(m/\kappa)$	NIW propagation w.r.t. horizontal	–
$\alpha = tan^{-1}(l/k)$	NIW propagation direction CCW from east	–
Φ	Phase of NIW w.r.t. September 13, 2018	–

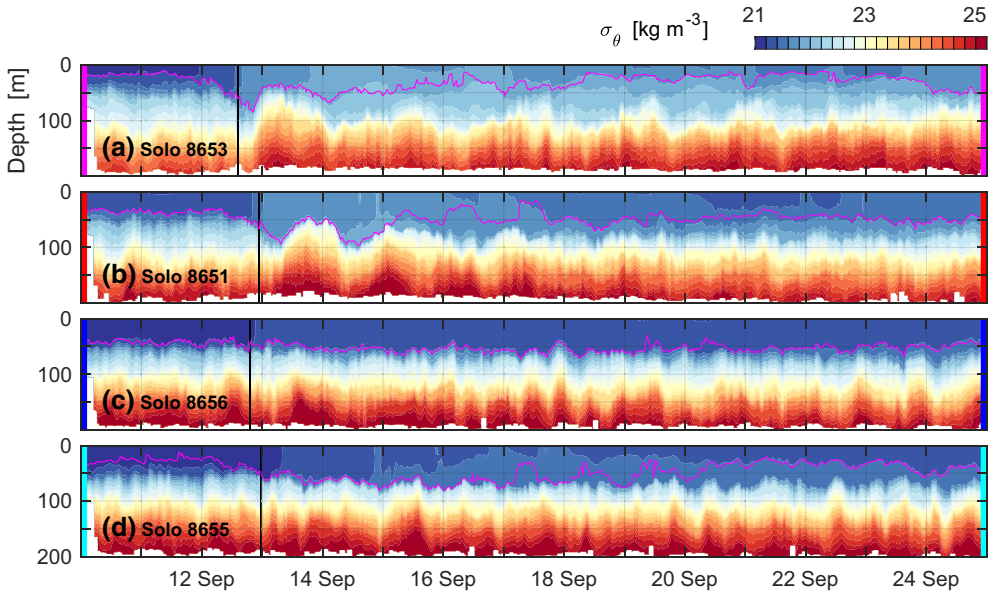

Figure 2. Potential density for floats (a) 8653, (b) 8651, (c) 8656, and (d) 8655. The mixed layer depth is about 50 m (pink line). The closest passage of the TC occurs near 0000 UTC on September 13 (vertical black line). Vertical bars at the ends of each panel reference each float's color in all figures.

3. Wind Power Input to the Mixed Layer from a High-Resolution TC Model

There were neither in situ measurements of winds nor currents over a wide area to the right of the TC. To estimate the total and NI wind input to the mixed layer, we use a high-resolution, coupled atmosphere-ocean modeling system to simulate Super Typhoon Mangkhut. We then use the model output to calculate the NI vertical energy flux and the fraction of mixed layer energy transported into the interior.

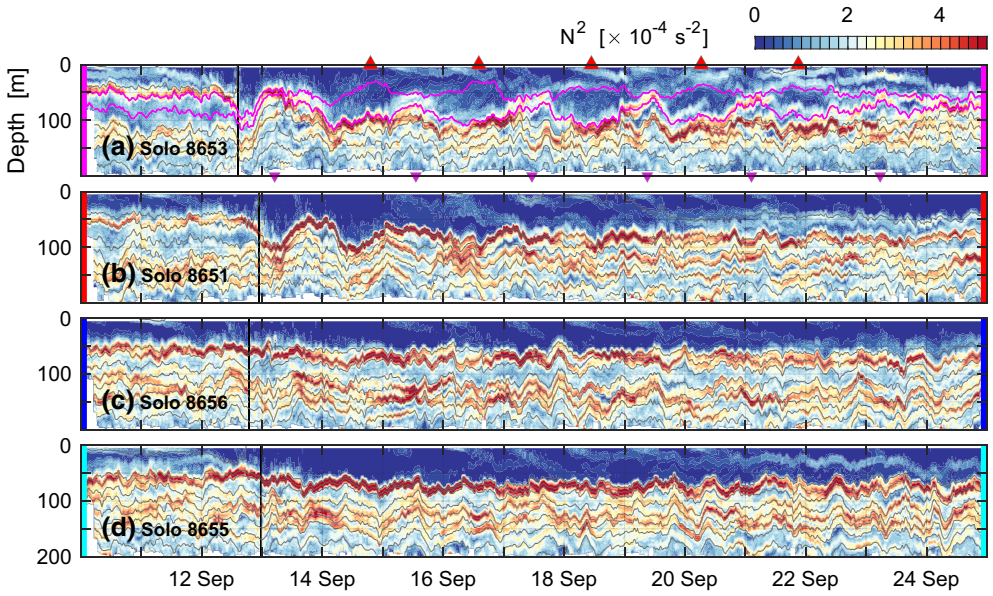

Figure 3. Buoyancy frequency squared is smoothed with an 11-m vertical running mean for floats (a) 8653, (b) 8651, (c) 8656, and (d) 8655. Isopycnals are contoured every 0.5 kg m^{-3} (gray and pink contours). The pink contours highlight straining above the N^2 maximum with times of high/low strain indicated by red/pink triangles.

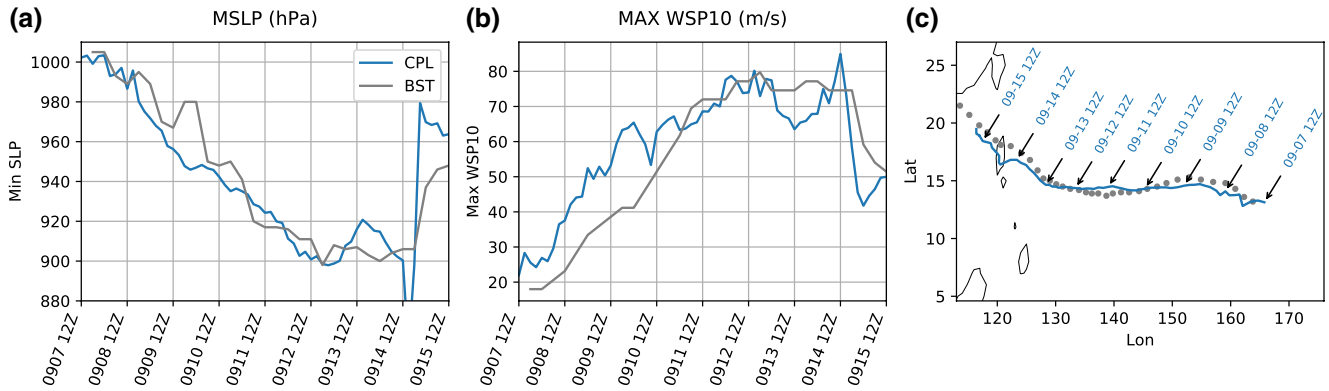

Figure 4. Coupled model results (blue) are compared to Joint Typhoon Warning Center track data (gray) for (a) the minimum sea level pressure, (b) maximum wind speed at 10 m, and (c) track.

The coupled system consists of two components: an atmospheric component, the Weather Research and Forecast (WRF) model V3.8.1 (Skamarock et al., 2008); and an oceanic component, the Hybrid Coordinate Ocean Model V2.2 (HYCOM; Wallcraft et al., 2009). The coupling method and its performance for TCs is documented by Chen and Curcic (2016) and Curcic et al. (2016). WRF and HYCOM exchange momentum and heat at the interface between the atmosphere and ocean. HYCOM also takes freshwater input from WRF-produced precipitation. SST evolves dynamically. The global HYCOM Global Ocean Forecasting System (GOFS) 3.1 reanalysis data, version GLBa0.08 93.0 is used to construct the initial conditions and lateral boundary conditions for HYCOM.

The computational domain of HYCOM covers the western Pacific, from 0.71°S to 29.76°N, 111.08°E to 179°E. The horizontal grid spacing is 0.08°. A total of 41 hybrid sigma vertical levels are used with 10 levels in the top 50 meters. The computational domain of WRF is slightly smaller than that of HYCOM. The WRF domain is discretized into 45 vertical levels, and a nominal top at 20 hPa. Three nested computational domains (D9, D3, and D1) are used with horizontal grid spacings of 9, 3, and 1 km. The total number of grid points in the atmosphere is $620 \times 230 \times 45$ (D9), $301 \times 301 \times 45$ (D3), and $401 \times 401 \times 45$ (D1).

The WRF model parameterizes several physical processes: shortwave and longwave radiative fluxes using the RRTMG scheme (Iacono et al., 2008); vertical turbulent eddy mixing using the YSU scheme (Hong et al., 2006); and surface and soil temperature over land using the NOAH MP land-surface physics scheme (Niu et al., 2011). The Morrison double moment scheme parameterizes cloud microphysics (Morrison et al., 2009). Surface fluxes are parameterized based on the Monin-Obukhov similarity theorem. No convective parameterization scheme is used. The numerical model is initialized at 0000 UTC on September 7, 2018. The ERA5 reanalysis (Hersbach et al., 2020) is used to construct the initial conditions and lateral boundary conditions for WRF. Spectral nudging toward the reanalysis data set is used in D9 to constrain the large-scale winds.

Our coupled numerical simulations are compared to Joint Typhoon Warning Center track data for Mangkhut (Section 2). The TC track and strength, as measured in minimum surface pressure and maximum wind speed, are reasonably reproduced (Figure 4). This favorable comparison gives us confidence to make further calculations.

At a single point, the energy flux from wind forcing into the total mixed layer kinetic energy is obtained without filtering for inertial motions (derived from Equation 1 in Plueddemann & Farrar, 2006):

$$P = \boldsymbol{U} \cdot \boldsymbol{\tau} \tag{1}$$

The wind stress ($\boldsymbol{\tau}$) is calculated using suitable drag coefficients for a TC, verified with TC observations (C. Davis et al., 2008), and acts on a uniform mixed layer velocity of $\boldsymbol{U}$, i.e., the slab model (Pollard & Millard, 1970). The mixed layer depth (h) may vary in space and time in either the observations or the model. Components are positive eastward and northward. P is largest mostly on the right side and in front

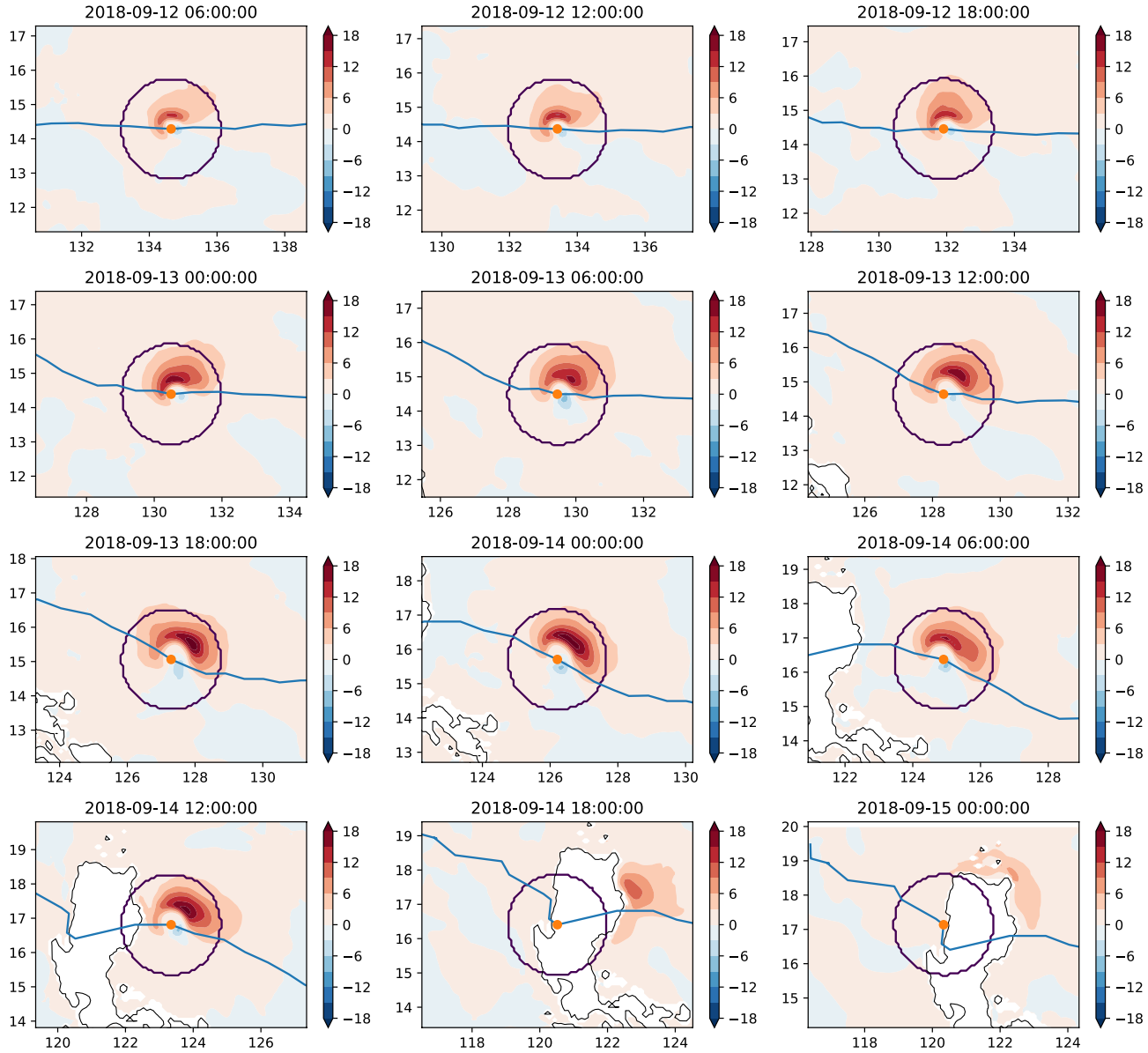

Figure 5. Snapshots of the energy flux from wind forcing into the total mixed layer kinetic energy (P in W m^{-2}) show it is stronger to the right of the TC. The simulated track (blue curve) is shown. An averaging radius of 1.5° (black circle) is used in Figure 6.

of/behind the TC before/after 0000 UTC 13 September. On the left side, P is small or marginally negative (Figure 5; Price, 1981). The total power averaged within 1.5° degrees of the TC is: $\langle P \rangle$ = 2.5–3.5 W m^{-2} on September 13, as it passed over the float array (Figures 1 and 6).

The energy flux from wind forcing to inertial kinetic energy in a mixed layer with a varying depth of h is (Equation 8 in Plueddemann & Farrar, 2006):

$$P' = -Re\left[\frac{\boldsymbol{U}'h}{if} \cdot \partial_t\left(\frac{\boldsymbol{\tau}}{h}\right)\right] \tag{2}$$

The NI mixed layer velocity is $\boldsymbol{U}'$, which is obtained from a third order Butterworth bandpass filter for $f \pm 25\%$. For a purely inertially-rotating $\boldsymbol{\tau}$ and constant h, a further simplification ensues, which is frequently used in the literature: $P' = \boldsymbol{U}' \cdot \boldsymbol{\tau}$. The area mean of Equation 2 within 1.5° degrees of the TC is:

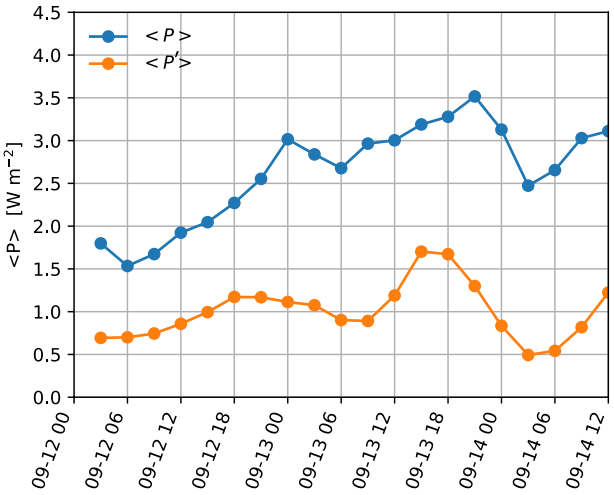

Figure 6. The area means of energy flux from wind forcing into the total and NI mixed layer kinetic energy, $\langle P \rangle$ (blue) and $\langle P' \rangle$ (orange), are obtained every 3 h within a 1.5° radius of the TC (black circle, Figure 5).

$\langle P' \rangle = 0.9$–1.7 W m^{-2} on September 13 (orange line, Figure 6). The fraction of this flux radiated into the interior is calculated from the float data in Section 8.

4. Near-Inertial Waves from the Floats

We have calculated the NI energy input to the ocean by the TC using model output in the previous section with the ultimate goal of comparing it to the vertical energy flux of the NIWs using the float data. The first step is to isolate NIWs by bandpassing density and velocity, which is the focus of this section. Since the floats measure density profiles from 0 to 200 m, depth-mean velocity, and surface velocity, some intermediate steps are needed to estimate depth-dependent velocity from density via the polarization relations (Section 5). We then check its validity against the depth-mean and surface velocities and compare kinetic energy from the various measurements. Mesoscale vorticity and shear in the TC wake affect the frequency, wavelength, and vertical group velocity (Section 6). We also identify an interfacial wave in the transition layer as one other source of short-wavelength NIWs, which propagate vertically (Section 7). Lastly, with these intermediate steps completed and with directional harmonic fits to data from all 4 floats, we (a) identify the horizontal direction, horizontal wavelength, amplitude, and phase of the NIWs; (b) estimate the NI energy density in the waves; and (c) use the vertical group velocity to calculate the vertical NI energy flux (Section 8).

We use wavelet transforms to analyze the frequency content of a float's time series and to perform the NI bandpass (Johnston et al., 2015; Johnston et al., 2016). Wavelets are selective in both time and frequency (Kumar & Foufoula-Georgiou, 1997; Torrence & Compo, 1998), which is useful in the analysis of NIWs because of their intermittency due to changes in forcing, background conditions, or float position (Figure 7). Amplitudes (A) and phases (ϕ), as functions of depth and time (t), are obtained from a wavelet transform. Bandpassed data are reconstructed from these amplitudes and phases. In particular, the Morlet wavelet (a complex exponential within a Gaussian envelope) is optimal because it possesses a minimum product of

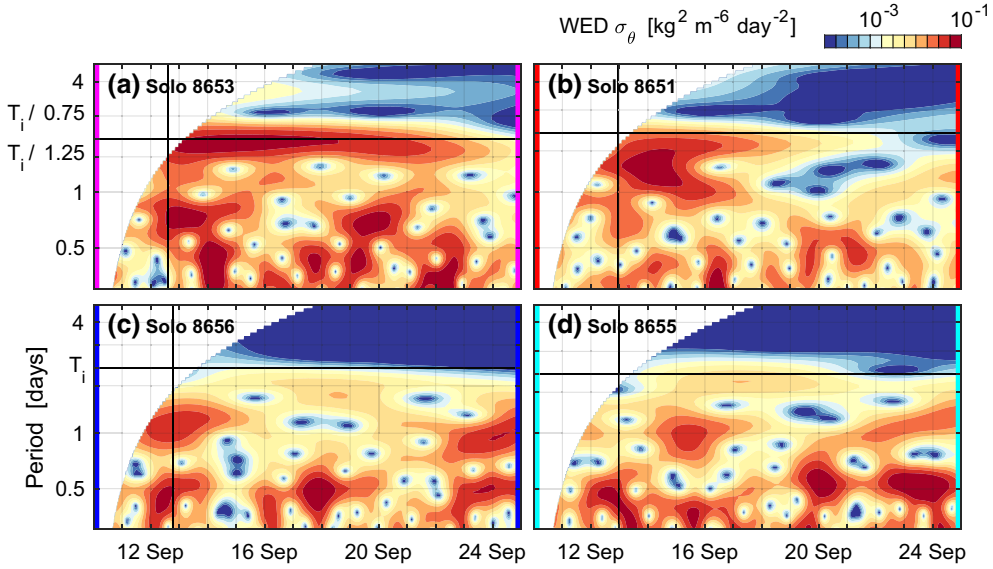

Figure 7. Scalograms of the wavelet energy density (WED) for potential density show its variance as a function of period and time. They are calculated at 110 m for floats (a) 8653, (b) 8651, (c) 8656, and (d) 8655. The NI bandpass is denoted around T_i (horizontal black line; additional gray lines for periods corresponding to $f \pm 25\%$). White space near the edges are masked for edge effects at the e-folding level, the duration of which increase with period.

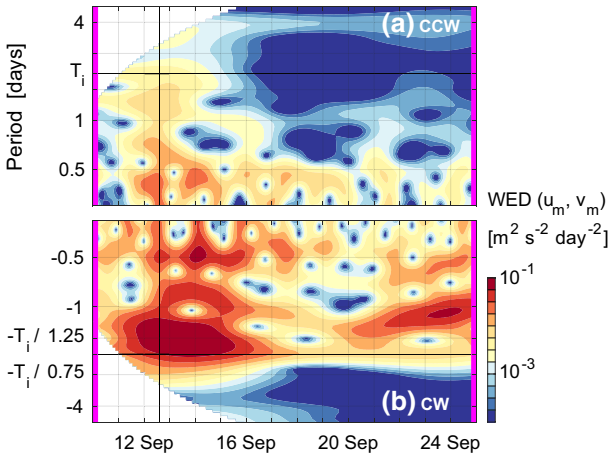

Figure 8. As in Figure 7, but for the depth-mean complex velocity from 0 to 200 m for Solo 8653. Variance as a function of time is separated into (a) positive period and counterclockwise rotation and (b) negative periods and clockwise rotation. Note the direction of increasingly positive period is the same in both plots.

the spreads in time and frequency. The full width of the envelope at the *e*-folding level is $2\sqrt{2}T_w$, where T_w is the period of the wavelet in question. Edge effects are removed within $1.5T_w$ days of the edges. Phases are referenced to 0000 UTC on Oct 1, 2018. Since profiles are irregularly spaced in time, they are interpolated to a regular grid of 1,000 s before this analysis.

Scalograms show variance as a function of time and period in terms of the wavelet energy density (WED), which is similar to power spectral density in Fourier analysis. To illustrate general features observed by the float array, we show representative scalograms at a depth of 110 m (Figure 7). Variance is substantially reduced for periods longer than T_i, a limit of the internal wave band. Variance is noted primarily at 0.5 days, 1 day, and T_i (which varies depending on the latitude of the float). For the 2 closest floats NI variance is largest after TC passage between T_i and $T_i/1.25$ (Figures 7a and 7b). The peak value of WED after the TC is at $\omega = 1.1f$, which we will use later in a NI bandpass. At the 2 distant floats, NI variance reaches a maximum 5 days after TC passage (Figures 7c and 7d). Since σ_θ is real, positive and negative periods are identical, but velocity is analyzed as a complex quantity and is therefore asymmetric as with Fourier transforms (Figures 7–8). We retain only the negative periods, which rotate clockwise with time like internal waves (Figure 8b; Leaman & Sanford, 1975).

Subinertial energy is at least an order of magnitude less than near f (Figures 7–8). Using wavelets, a lowpass of 4 days or about $2\,T_i$ is used to produce background density and stratification, which are denoted as: $\langle\sigma_\theta\rangle$ and $\langle N^2\rangle$. Since data are binned at 1 m, N^2 is noisy and so for these calculations we perform an 11-m running mean in the vertical to produce a smoothed result in time and depth: $\langle\langle N^2\rangle\rangle$.

NI energy from 1 to $1.25f$ is elevated for days after the passage of the TC (Figures 7 and 8). To isolate NIWs, data are bandpassed for $\omega = f \pm 25\%$. Primes denote bandpassed data (i.e., σ_θ'; Figure 9). Then, NI vertical displacements are calculated: $\eta(z, t) = -\sigma_\theta'/\partial_z\langle\sigma_\theta\rangle$. The total NI energy is:

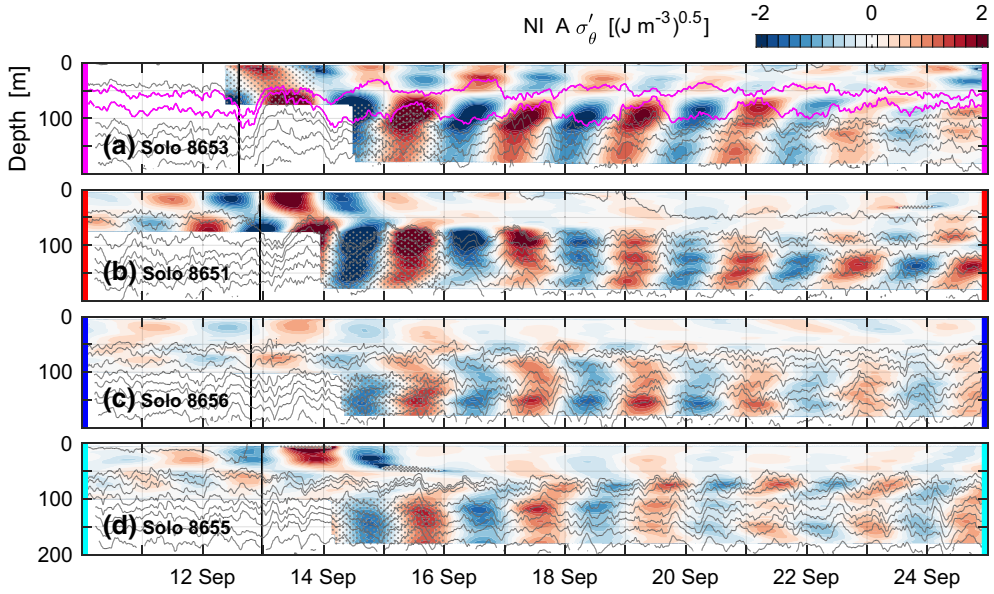

Figure 9. The amplitudes of the NI density fluctuations are scaled ($A\sigma_\theta'$) to equal E_p when squared (Equation 4) for floats (a) 8653, (b) 8651, (c) 8656, and (d) 8655. Isopycnals are contoured every 0.5 kg m^{-3} (gray or pink contours). Stippled areas denote influence of edge effects from calculations of lowpassed variables: $\langle\sigma_\theta\rangle$ and $\langle N^2\rangle$. NI, near-inertial.

$$E(z,t) = E_k(z,t) + E_p(z,t) = \frac{\langle \sigma_\theta \rangle}{4}\left(A_u^2 + A_v^2\right) + \frac{\langle \sigma_\theta \rangle}{4}\langle\langle N^2 \rangle\rangle A_\eta^2 \quad (3)$$

E_k is the sum of terms 1 and 2. The third term is potential energy (E_p), which can also be written as:

$$E_p(z,t) = (\sigma_\theta' g)^2 \,/\, \left(4\langle \sigma_\theta \rangle \langle\langle N^2 \rangle\rangle\right) = (A\sigma_\theta')^2 \quad (4)$$

E_p derives from profiles of σ_θ', while our measured E_k comes from either $\mathbf{u_m}$ or $\mathbf{u_s}$. We refer to these as E_{km} and E_{ks}. In Section 5, we obtain depth-varying velocities from σ_θ' via the internal wave polarization relations and a depth-varying kinetic energy based on these velocities, which we refer to as $E_{k\sigma}$. NI $A\sigma_\theta'$ is a scaled displacement (Figure 9) and its vertical derivative is a scaled strain, $\partial_z(A\sigma_\theta')$. We return to the latter quantity in Section 7 to identify vertical propagation, while the former is useful in visualizing NIW fluctuations amidst varying stratification in the next section.

The vertical energy flux magnitude is:

$$F_z(z,t) = c_{gz}E \quad (5)$$

NIWs are generated by storms and have initial horizontal scales comparable to the storm and $\omega \sim f$, which imply slow downward propagation. We return to NI energy propagation after estimating depth-varying velocity in the next section.

5. Estimating Depth-dependent, Near-Inertial Velocity

To calculate NI F_z, we require depth-varying velocity and E_k. Since the floats measure only $\mathbf{u_m}$ and $\mathbf{u_s}$, we estimate the NI depth-varying velocity for a wave propagating southward via the polarization relations for internal waves (Gill, 1982):

$$w' = A_w e^{i(\mathbf{k}\cdot\mathbf{x} - \omega t)} \quad (6)$$

$$\sigma_\theta' = i\langle \sigma_\theta \rangle \langle\langle N^2 \rangle\rangle w' \,/\, (g\omega) \quad (7)$$

$$v' = -w' \tan\theta \quad (8)$$

$$u' = -iv' f \,/\, \omega \quad (9)$$

where the vertical velocity is w with an amplitude of A_w and the position is $\mathbf{x} = (x, y, z)$ with respect to the origin at 14.5°N, 132.5°E and the sea surface. The wavenumber is $\mathbf{k} = (k, l, m) = (0, l, m)$. The magnitude of the horizontal wavenumber is given by: $\kappa = \sqrt{k^2 + l^2} = 2\pi/\lambda_h$. The vertical wavenumber is $m = 2\pi/\lambda_v$. Components are positive eastward, northward and upward. The wavenumber angle from the horizontal is given by the dispersion relation:

$$\tan^2\theta = m^2 \,/\, \kappa^2 = (\langle\langle N^2 \rangle\rangle - \omega^2) \,/\, (\omega^2 - f^2) \quad (10)$$

with $\omega = 1.1f$ (the WED maximum after the TC in Figure 7a) and the measured σ_θ', we obtain estimates of depth-dependent velocity:

$$\mathbf{u}_\sigma' = (u_\sigma', v_\sigma') = (fH \,/\, \omega, iH)\sigma_\theta' \quad (11)$$

from Equations 6 to 9 (Figure 10). We emphasize that this depth-dependent velocity is not measured, but depends on several processing steps and assumptions. Where a σ subscript appears, such as $E_{k\sigma}$, it denotes reliance on this or similar estimates, which follow. The transfer function is:

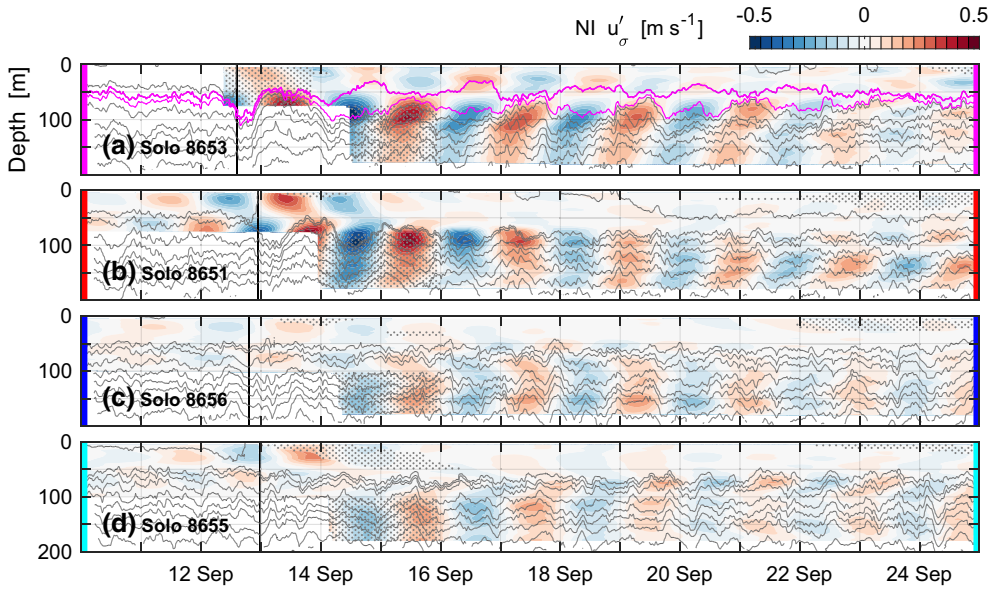

Figure 10. As in Figure 9, but for the estimate of NI eastward velocity, which is calculated from the polarization relations based on the measured NI bandpassed potential density (σ_θ'; Equation 11) for floats (a) 8653, (b) 8651, (c) 8656, and (d) 8655. NI, near-inertial.

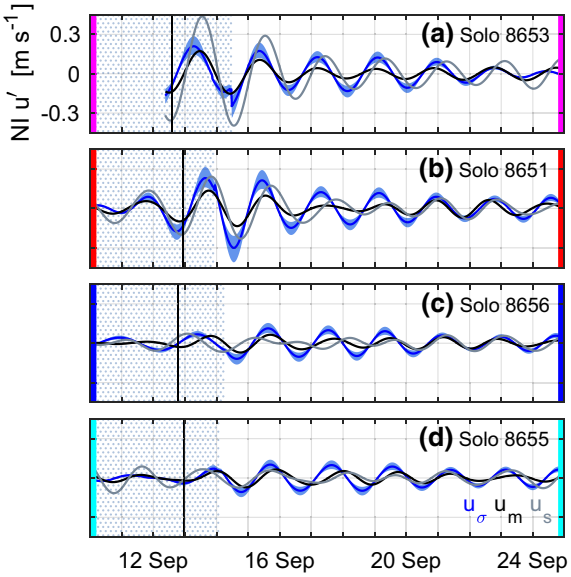

Figure 11. Observed NI depth-mean eastward velocity from 0–200 m (u_m, black line) and surface velocity (u_s, gray line) are compared to the depth-mean of the estimated NI depth-varying velocity (u_σ', blue line at $\omega = 1.1f$ with light blue shading for $\omega = 1.05$–$1.25f$) for floats (a) 8653, (b) 8651, (c) 8656, and (d) 8655. Stippled areas denote NI u_σ' and u_m' are calculated over different depth ranges (floats are profiling to ~200 m, but edge effects limit calculation of u_σ' below 75–100 m from 10 to 14 September; Figure 10). NI, near-inertial.

$$H(\omega) = \frac{g\omega \tan\theta}{\langle\sigma_\theta\rangle\langle\langle N^2\rangle\rangle} \tag{12}$$

For the real components of a southward propagating wave, the transverse velocity (u') is in phase with σ_θ' (Equations 6–9), which appears to be the case (Figures 9 and 10). The measured value of NI u'_m is usually in phase with the inferred depth-mean of u'_σ for the 2 closest floats (Figures 11a and 11b). The southward propagation is confirmed by directional fits in Section 8.

Next we estimate depth-varying E_k from E_p because the floats do not measure velocity profiles. NIWs have flat aspect ratios and E_k is greater than E_p (Equation 10). Their ratio is:

$$R_\omega = E_k / E_p = (\omega^2 + f^2) / (\omega^2 - f^2) \tag{13}$$

Therefore, R_ω and H are sensitive to ω near f, as are our estimates of $\mathbf{u}'_\sigma$ and $E_{k\sigma}$. With $\omega = 1.06$, 1.10, and $1.25f$, $R_\omega = 17$, 11, and 5.5. These are changes of 63/43% for $\omega = 1.06f/1.25f$ compared to the value of $1.1f$ at the mean latitude of the float array, 14.3°N (Table 2). By comparing the depth-mean of depth-dependent u'_σ estimates to the observed u'_m, we can gauge our methods (Figure 11). Lastly, we note some additional details of energy calculations. The depth-mean E_k derived from $\mathbf{u}'_m$ is:

$$E_{km}(t) = \langle\sigma_\theta\rangle\left(A_{um}^2 + A_{vm}^2\right) / 4 \tag{14}$$

and similarly for E_k at the surface: $E_{ks}(t)$. A_{um} is the bandpassed amplitude for u_m and similarly for v_m. We calculate depth-varying E_k from E_p (Equation 4) and the dispersion relation at $\omega = 1.10$ and $1.25f$ (Equation 13):

$$E_{k\sigma}(z,t) = R_\omega E_p(z,t) \tag{15}$$

Table 2
Wave Properties (λ_v, R_ω, and c_{gz}) are Calculated From Equations 10, 13, and 16 for Waves With $\omega = 1.1f$ or $1.25f$ and a Given λ_h.

λ_h	λ_v	$\partial_z v$			c_{gz}	Δt	τ_e
[km]	[m]	[$\times 10^{-3}$ s^{-1}]	ω/f	R_ω	[m day^{-1}]	[days]	[days]
500	577	0	1.10	11	53	2.8	3.5–7.0
500	577	1.5	1.25	4	73	2.1	2.5–5.0
750	866	0	1.10	11	80	1.9	2.3–4.6
750	866	1.5	1.25	4	109	1.4	1.7–3.4
1,000	1,155	0	1.10	11	107	1.4	1.7–3.4
1,000	1,155	1.5	1.25	4	145	1.0	1.3–2.6

For waves in a background shear ($\partial_z v$), changes in ω and c_{gz} are obtained from Equations 19 to 20. The time for energy to propagate in the vertical is $\Delta t = c_{gz}\Delta z$, where $\Delta z = 150$ m. τ_e is an estimate from Equation 18, where the factor of 2 arises from 2 depth ranges considered: $\Delta z = 150$ m or 300 m.

Next we evaluate our estimate of depth-varying NI velocity: u'_σ. At the closest float to the TC, NI motions have upward phase propagation below the mixed layer, which implies downward energy propagation (Figures 9a and 10a). At the other 3 floats, there is a combination of up- and downward phase propagation or limited phase propagation with depth (Figures 9b–9d and 10b–d). σ_θ' variations imply $u'_\sigma > 0.5$ m s^{-1} at the two closest floats to the TC (Equation 11; Figures 10a and 10b) and about half that at the 2 distant floats (Figures 10c and 10d). Often there is a sign change in the NI motions from the mixed layer into the thermocline at about 50 m (Figures 9 and 10). This shear will reduce the depth-mean value and E_{km} will underestimate the actual depth-mean E_k (Figure 12). The observed u_s' is comparable to the depth-mean of the estimated u'_σ, which can be about twice u_m' (Figure 11). Based on the similar phase from September 13–16 between u'_σ and u_m', the NIW is propagating southward. Prior to September 14, the bandpass does not cover the full profiling range because of edge effects within $1.5T_i$ and so there is a mismatch between the depth ranges of the depth-mean velocities (stippled region in Figures 10 and 11). Overall, there is reasonable agreement between NI u_m' and depth-mean u'_σ, but the former underestimates the NI amplitude due to vertical shear of the NIW.

6. Vertical Propagation Though Mesoscale Vorticity and Shear

In this and the following section, we examine 3 processes that increase c_{gz}: (a) mesoscale vorticity in the TC wake, (b) mesoscale shear in the wake, and (c) generation of secondary NIW with shorter horizontal wavelengths. The mesoscale is at scales of 100–200 km compared to horizontal wavelengths of 500–1,000 km for the NIWs (Section 8). Since our central $\omega = 1.1f$ is quite large compared to typical values of storm-generated NIWs within several percent of f (Alford et al., 2016), we also examine if our observed ω is consistent with the background shear and vorticity. It is well-established, that (a) inertial motions at larger ω arise amidst mesoscale cyclonic vorticity and (b) mesoscale vertical shear of the background flow alters the dispersion relation and ω (Pallàs-Sanz et al., 2016). Once we calculate τ_e for NI E_k from Figure 12 below, we can compare that value to the estimated τ_e required for NIWs to propagate out of the upper ocean amidst mesoscale vorticity and shear (Table 2). Doppler shifting by the background flow does not apply here since the floats are drifting with the flow, but an NIW's observed Eulerian frequency is: $\omega_o = \omega - k\langle u\rangle$, where the mean flow is $\langle u\rangle = 0.5$ m s^{-1} (i.e., the NEC; Section 7). For $\lambda_h = 500$–1,000 km, the $\omega_o - \omega$ difference is notable at 0.09–$0.17f$.

The closest (pink) float on the right side of the TC and in the cold wake accelerates relative to the next closest (red), which indicates a mesoscale cyclonic relative vorticity between the 2 closest floats (Figure 1). With a separation between the floats of 200/100 km during/after passage of the TC (on 13/18 September), we approximate this mesoscale relative vorticity as $\zeta \approx \partial_y\langle u\rangle$ from both u_s and u_m (Figures 13b and 13c). (Given the zonal orientation of the cold wake, we neglect $\partial_x\langle v\rangle$, which is an order of magnitude smaller than $\partial_y u$.) $\zeta_{s/m}$ is $0.3f/0.2f$ one day after the TC. Therefore, the effective Coriolis frequency is: $f_e = f + \zeta_{s/m}/2 = 1.15f/1.10f$ (Kunze, 1985). Four days after the TC, the vorticity reduces to $0.1f$. Thus, vorticity is elevated over 200 km for about one T_i, which are scales relevant to NIW generation (Pallàs-Sanz et al., 2016).

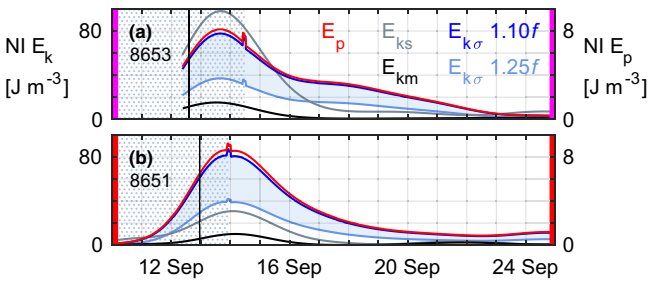

Figure 12. NI kinetic energy (E_k) is calculated for floats (a) 8653 and (b) 8651 using 2 methods. NI E_{ks} (black line) and E_{km} (gray line) are calculated directly from observed depth-mean and surface NI currents (NI $\boldsymbol{u_m'}$ and $\boldsymbol{u_s'}$ from Figure 11). NI $E_{k\sigma}$ (blue line at $\omega = 1.1f$, light blue for $\omega = 1.25f$) is estimated from the depth-varying NI potential energy (E_p, red line, right axis) and then averaged in depth. Stippled areas are from Figure 11. NI, near-inertial.

Vertical energy propagation for a hydrostatic, rotating wave in a quiescent ocean is determined by the vertical group velocity (Equation 5):

$$c_{gz} = -N^2\kappa^2 \Big/ \left[m^2\sqrt{f^2m^2 + N^2\left(\kappa^2\right)}\right] \tag{16}$$

At $\omega \sim f$, motions are nearly horizontal, at κ comparable to that of the wind stress, and have $c_{gz} \sim 0$. If instead due to mesoscale vorticity, the

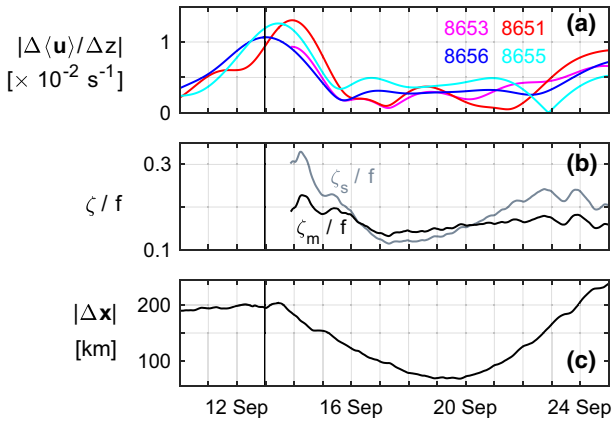

Figure 13. (a) The magnitude of the mean shear ($|\Delta u/\Delta z|$) peaks with TC passage and then decreases for all 4 floats (Equation 21). (b) Cyclonic relative vorticity is normalized as ζ/f, peaks with TC passage, and then decreases. ζ is calculated from the surface and depth-mean velocities (gray and black lines) for the 2 closest floats, 8653 and 8651. (c) The separation distance of the 2 closest floats shows ζ is at mesoscale. TC, tropical cyclone.

NIWs are generated near the surface at $\omega = f_e = 1.1f$ and reach a quiescent interior without vorticity and geostrophic shear, c_{gz} is 53–107 m day^{-1} for λ_h of 500–1,000 km, which moves energy across the stratified interior region of ~50–200 m depths in Δt = 1.0–2.8 days (Table 2).

The observed E_k decays exponentially at the floats (Figure 12), which will be compared below to decay scales modified by mesoscale shear and vorticity. We can calculate an e-folding decay scale as follows. Assuming the change in E over time is due only to vertical flux divergence over the layer in question:

$$\partial_t E = -\partial_z F_z = -\frac{E_o}{\tau_e} e^{-t/\tau_e} \tag{17}$$

where the initial energy density is E_o = 80 J m^{-3} (Figure 12). From the initial rate of exponential decay, the decay scale is:

$$\tau_e = E_o \,/\, \partial_z F_z \tag{18}$$

We calculate F_z based on various c_{gz} (Equation 5 and Table 2). $\partial_z F_z$ is estimated as follows: $F_z = 0$ in the mixed layer (0–50 m) and we assume the divergence takes place over the next 150 m. We obtain τ_e = 1.3–3.5 days for the range of c_{gz} in Table 2. If the divergence occurs over 300 m instead, τ_e doubles to 2.6–7.0 days.

For the closest float, there appear to be 2 time scales (Figure 12a), which are obtained over 2 fitting intervals to Equation 17 from 14 to 16 September and September 16–21. The next closest float is fit from 14 to 21 September (Figure 12b). The variance explained by the fits exceeds 95%. τ_e is 2.9 days for float 8651 and is initially 2.7 days for float 8653 (Figure 12), which is consistent with values for NIWs with λ_h = 500–1,000 km amidst mesoscale vorticity and shear (Table 2). This topic is covered in the next paragraph. The secondary decay for the closest float is τ_e = 5.0 days and may be related to shorter waves, which are generated in the transition layer well after the TC (Section 7). To confirm these values of λ_h, we will turn to an assessment of the data from the float array as a whole in Section 8.

Once a NIW propagates downward out of the mixed layer, vertical shear of geostrophic currents (u_g, v_g) alters isopycnal slopes, the effective N^2 encountered by NI motions, and thereby modifies both the dispersion relation and c_{gz} (Kunze, 1985):

$$\omega \simeq f_e + N^2\kappa^2 \,/\, (2fm^2) + \partial_z(u_g, v_g) \cdot (l, -k) \,/\, m \tag{19}$$

$$c_{gz} \simeq -N^2\kappa^2 \,/\, (fm^3) - \partial_z(u_g, v_g) \cdot (l, -k) \,/\, m^2 \tag{20}$$

At 13–15°N, the 4-year mean speed of the NEC from geostrophy is ~0.2 m s^{-1} westward in the upper 200 m (from Figure 4 in Schönau & Rudnick, 2015), but instantaneous values of the current can reach 0.6 m s^{-1} with shear ~4×10^{-3} s^{-1}. Next, we compare this value to estimates from the floats, which lack direct measurement of depth-dependent velocity. We assume three layers with (a) uniform u_s in the mixed layer (its depth is h), (b) uniform shear over the transition layer (its width is b = 30 m) between the mixed layer and thermocline, and (c) uniform velocity in the thermocline (from $b + h$ to the maximum profile depth, H). These assumptions combined with the low passed, measured values of u_s and u_m yield an estimate for the mean shear (N. Brizuela, pers. comm.):

$$\frac{\Delta\langle \mathbf{u} \rangle}{\Delta z} = (\langle \mathbf{u_s} \rangle - \langle \mathbf{u_m} \rangle) \frac{2H}{b^2 + 2b(H - b - h)} \tag{21}$$

Peak shear from the floats is mainly from the eastward component on 13 September, exceeds 0.01 s^{-1}, and relaxes to 1–5×10^{-3} s^{-1} after the TC, which is consistent with glider-based thermal wind shear (Figure 13a). The depth-mean value of N^2 is 2×10^{-4} s^{-2}.

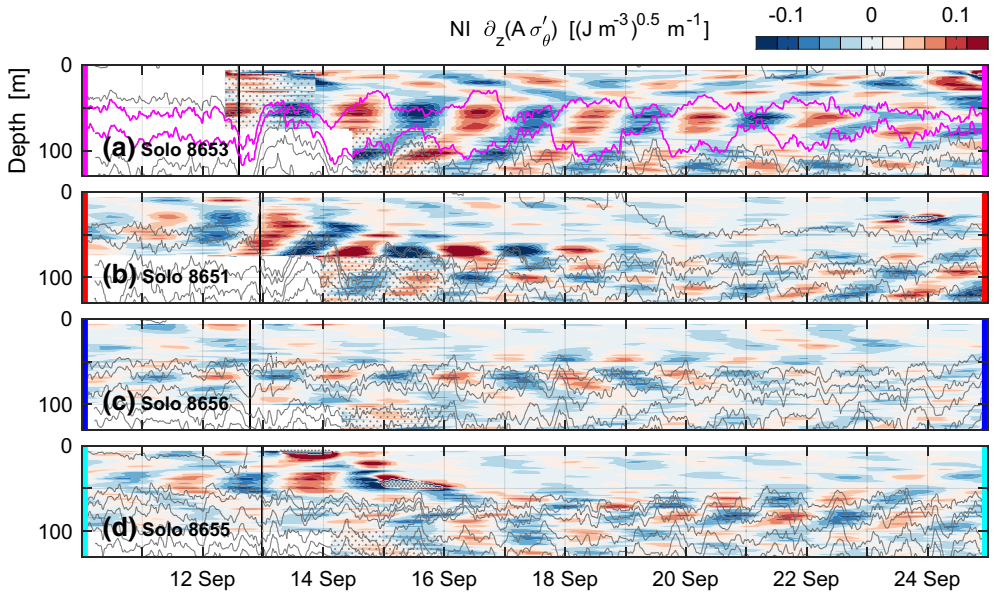

Figure 14. As in Figure 9, but a scaled strain highlights vertically-propagating signals and is calculated as $\partial_z(A\sigma_\theta')$, where scaled NI potential density ($A\sigma_\theta'$) resembles E_p when squared for floats (a) 8653, (b) 8651, (c) 8656, and (d) 8655. NI, near-inertial.

Lastly to estimate c_{gz}, we require (k, l, m), which are estimated as 2π/(500–1,000 km, 0, 577–1,155 m). (k, l) are obtained from directional fits to all the float data in Section 8, while λ_v appears to be somewhat larger than the profiling depth at times (based on depths of zero crossings in Figure 9a) and is the most poorly estimated value in this calculation. Values of m are calculated from the dispersion relation in the absence of shear (Equation 10) based on k and $\omega = 1.1f$. Using these wavenumbers values with $\partial_z v = 1.5 \times 10^{-3}$ s^{-1} and $f_e = 1.1f$ yields $\omega = 1.25f$ and $c_{gz} \sim$ 73–145 m day^{-1} with larger values for larger λ_h. Stronger shear is noted (Figure 13a) and would further increase c_{gz}. However, the observed $\omega = 1$–$1.25f$ (Figure 7) is consistent with the level of shear used in Table 2. With this c_{gz}, a NIW propagates 150 m deeper in 1.0–2.1 days for λ_h = 500–1,000 km, which is somewhat faster than in the absence of shear (1.4–2.8 days).

In summary, the exponential decay of NI energy has τ_e = 2.7–2.9 days for the 2 closest floats and is consistent with NIWs generated amidst mesoscale vorticity and shear (Figure 12 and Table 2). In the following section, we note the ongoing generation of NIWs in the transition layer, which may contribute to a longer τ_e = 5.0 days at a later time for the closest float. The comparison for the longer decay time is complicated by the passage of Super Typhoon Trami on 23 September (Johnston et al., 2020), which although more distant may have generated further NIWs (Figures 7–11). The two northern floats (red and pink) were within 500 km of Trami and under tropical storm winds (18–32 m s^{-1}).

7. An Interfacial Near-Inertial Internal Wave

In this section, we examine one more process enhancing vertical propagation of energy by NIWs. A NIW between 50 m and 100 m resembles a mode-2 interfacial wave, as isopycnals alternately dilate and compress (pink contours, Figure 14a). In other words, in a vertical mode-2 structure, a crest in the upper layer lies over a trough in the lower layer, which in this case is a 180° phase shift in σ_θ' and u' across the transition layer (Figures 9a and 10a). The phase shift for the other floats is highlighted better by the gradient, which emphasizes higher wavenumbers (Figure 14). Such shear and strain in the transition layer may contribute to mixing. For the two closest floats but especially so for the closest float (pink), the interfacial wave strains isopycnals between σ_θ = 22 and 22.5 kg m^{-3} (pink contours) from 14 to 23 September. A weaker strain appears for the two distant floats, which is best seen in Figures 3c and 3d. $\partial_z(A\sigma_\theta')$ is also used to follow phase propagation (Figures 14a and 14b). Phase propagates up-/downwards in the interior/mixed layer and, therefore, energy propagates down-/upwards. These results suggest this process occurs mainly in the wake.

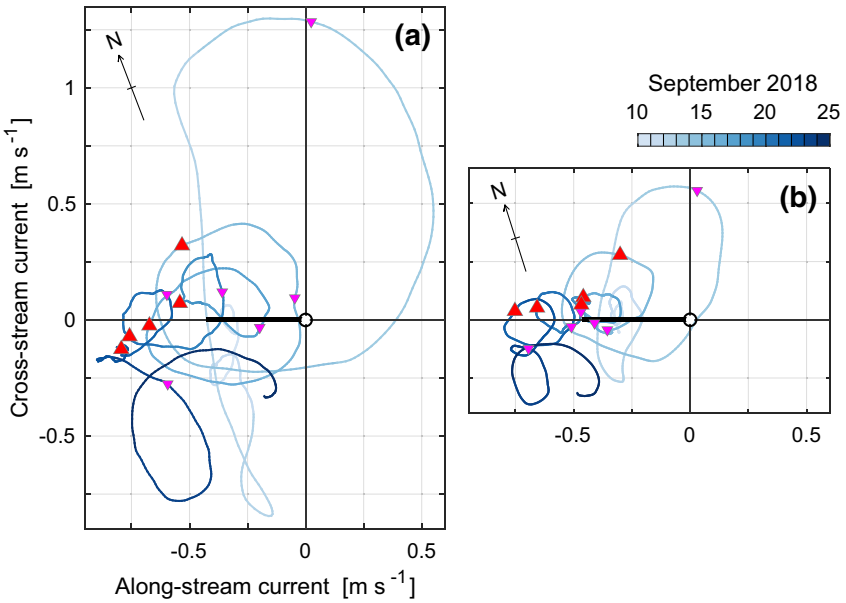

Figure 15. A hodograph of (a) surface and (b) depth-mean velocities from 0–200 m for float 8653 shows the contribution of the mean flow in the NEC and oscillating flow from NIW. Velocities are rotated into along-stream and cross-stream current defined by the mean current of about 0.5 m s^{-1}, which is roughly westward from 13 to 25 September (thick black vector). Velocities are smoothed over 14 h. The line color indicates date. Red/pink triangles show maxima/minima of strain occur every inertial period for local maximum/minimum westward flow (Figure 3a). A compass rose indicates north and the rotation. NEC, North Equatorial Current; NIW, near-inertial internal waves.

Next, we examine λ_h of this interfacial wave. In Section 8, directional wave fits will show a westward propagating wave with $\lambda_h \approx$ 50–100 km. The mean N^2 below 50 m, where NIWs propagate downwards, is 2×10^{-4} s^{-2} (Figures 3 and 14). With $\lambda_v \approx$ 125 m and $\omega = 1.1f$–$1.25f$ (Figures 7a and 8b), the dispersion relation yields $\lambda_h \approx$ 65–108 km in this lower layer (Equation 10), which is consistent with the values of 50–100 km.

The secondary NIWs are generated by either (a) the vertical displacement of the stratified layer or (b) advection of such displacements across a stratified fluid, which resembles the mechanism for the generation of internal waves by flow over sinusoidal topography (Bell, 1975; Bell, 1978). In the former case, with a mean N^2 above 50 m in the mixed layer of 0.5×10^{-4} s^{-2} and $\lambda_v \approx$ 40 m, the dispersion relation yields $\lambda_h \approx$ 10–17 km, which is too short. For the latter case of flow over the topography of the transition layer (i.e., its isopycnal displacements), $k = \omega/\langle u \rangle$, where the mean NEC flow is $\langle u \rangle = 0.5$ m s^{-1} (Figure 15) and $\omega = 1.1f$–$1.25f$, in which case $\lambda_h =$ 69–79 km. This value overlaps with that of the interfacial wave, which suggests the secondary NIWs are generated by this process. Internal wave generation in the transition layer by this obstacle mechanism has been noted previously for near-N waves (Czeschel & Eden, 2019; Polton et al., 2008) and for eddies obstructing NI flow (Bell, 1978).

The interfacial wave alternately dilated and compressed two isopycnals (pink contours; Figure 3a), which reduced and increased N^2. We examine the timing of this strain with respect to the combined flow in the NEC and NIWs. The closest float drifts roughly westward in the mean NEC flow (pink trajectory in Figure 1) with small loops in its trajectory due to NIW. The strain increases/decreases, when NI u' augments/opposes the westward mean flow leading to divergence/convergence in the mixed layer. This process is verified by determining where the strain occurs in a hodograph of along- and cross-stream velocities (Figure 15). The coordinate rotation is based on the mean flow from after TC passage from September 13–25 (black along-stream current vector in Figure 15). Maximum strain occurs near the time of maximum along-stream surface flow in each of the 5 inertial periods following the TC (red triangles indicate maximum strain every T_i in Figures 3a and 15a), while the middle 4 instances of minimum strain occur when the NI u' opposes the mean current (pink triangles indicate minimum strain in Figures 3a and 15a). These strain extrema are determined from the difference of the 14-h smoothed depths of the 22 and 22.5 kg m^{-3} isopycnals. A similar situation is noted for the depth-mean currents (Figure 15b). Thus, this process occurs only for NI motions in

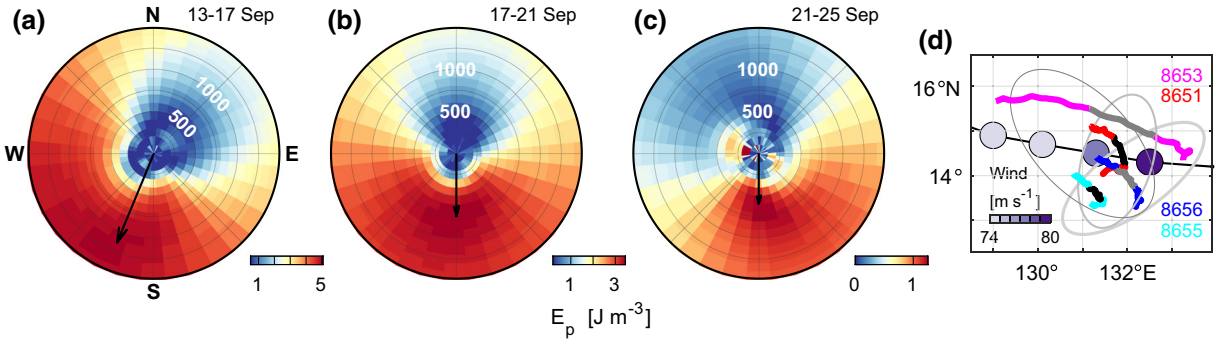

Figure 16. The direction, wavelength, and amplitude of propagating NIWs are obtained from harmonic fits of all 4 floats' potential density. The mean amplitudes from 120 to 179 m are squared and scaled to form NI potential energy (E_p; Equation 4). The fits are at $\omega = 1.1f$ for varying $\boldsymbol{k}$ in 4-days segments from (a) 13 to 17 (b) 17 to 21, and (c) 21 to 25 September. Southward propagation at wavelengths from ~500–1,000 km is noted from the maximum amplitude (black vector). (d) Float locations for each 4-days segment are shown (alternating gray/colored lines) with the orientation of the float antenna indicated (gray ellipses). The TC location is shown at 6-h intervals starting at 1800 UTC on 12 September with the dot color/size indicating the maximum wind speed/radius. NI, NI, near-inertial; NIW, near-inertial internal waves; TC, tropical cyclones.

a mean flow of similar speed and reinforces isopycnal displacements, which lead to up-/downward energy propagation from the transition layer into the mixed layer/thermocline.

8. Directional Wave Fits

To this point, we have used the data from each float individually. Here, we combine the data from the entire array to examine the evolution of wave properties after the TC, such as amplitude and horizontal wavenumber (i.e., both λ_h and propagation direction). In particular, we look for evidence of decreasing λ_h over time, which indicates faster vertical propagation (Equations 16 and 20). As an antenna, the array identifies coherent NIWs via harmonic fits in space and time similar to studies of internal tides from altimetry and gliders (Johnston et al., 2015; Zhao et al., 2018). σ_θ is fit over a 4-days interval or about two T_i because of the changing forcing and changing float configurations (Figure 16d). We fit the the wave to a single wavenumber at a time as: $A_\sigma \exp[i(\mathbf{k}\cdot\mathbf{x} - \omega t - \phi)]$ at $\omega = 1.1f$. Propagation direction is $\alpha = tan^{-1}(l/k)$ and so east, north, west, and south correspond to $\alpha = 0°$, 90°, 180°, and −90°. The phase (ϕ) is defined with respect to September 13, 2018. To perform the fit at each depth, $\mathbf{k}$ is specified for each λ_h from 50 to 1,500 km in 50-km intervals and each α from 0–360° in 11.25° intervals (Figures 16a–16c). Finally, we take the depth-mean value of A_σ from 120–179 m, use its maximum to determine λ_h and α, and plot it as E_p (black vector, Figures 16a–16c; Equation 4). Similar results for λ_h, ϕ, and E_p are obtained for the three different averaging depth ranges: 60–179, 60–119, and 120–179 m, but we concentrate on the latter depth range for clarity (Figures 17b–17d). In summary, all 4 floats are used to obtain values of A_σ (plotted as E_p) and $\mathbf{k}$ for waves, which are coherent over the area covered by the array (Figure 16d). In addition, a similar process was applied to $\mathbf{u_m}$ and E_{km}. Sensitivity tests of this method to $\mathbf{k}$ are performed (Figures S1–S3), as the float configuration varies over time (Figure 16d).

For three 4-day segments, E_p and λ_h decrease, while α remains between south-southwestward and southward (Figures 16a–16c). These trends are confirmed by performing 4-days fits for the intervening times and constructing a time series (Figure 17a). E_p was maximum on September 14, 1 day after the passage of Super Typhoon Mangkhut (Figure 16d). There is a quick decay almost to pre-TC levels followed by a prolonged decay until the passage of Super Typhoon Trami on September 23 (Johnston et al., 2020). These two stages were noted in Section 6 with $\tau_e = 2.7$ days and 5.0 days. ϕ was steady until September 21 (and possible effects ahead of Trami), which suggests the antenna indeed identifies a coherent wave, even as the float configuration evolves over time (Figure 17c).

Our estimates of horizontal wavelength are compared to previous work and estimates of length scales based on TC characteristics. With their mooring array, Pallàs-Sanz et al. (2016) find λ_h increases from about 400 km near the surface to 1,000 km at depth, as the wave propagated downwards. Our estimate of λ_h was a maximum of 1,150 km and decreased to 500 km with considerable variability over time (Figure 17b).

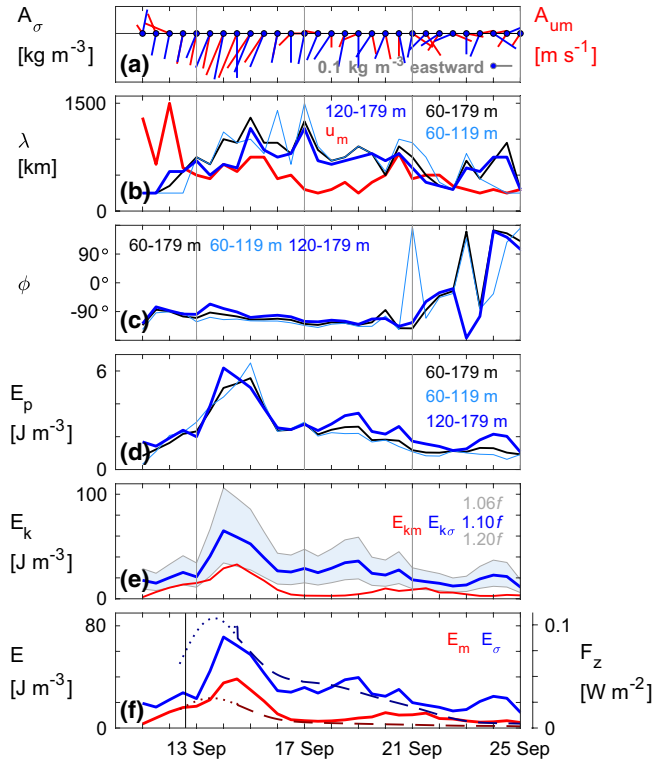

Figure 17. By repeating the fits in Figure 16 at intervening, overlapping 4-day intervals, time series of NIW amplitudes, horizontal wavelengths, horizontal propagation direction, phases, energy density, and vertical energy flux are obtained from the float array at $\omega = 1.1f$. (a) NIW amplitudes of potential density (depth-mean A_σ from 120 to 179 m, blue) and depth-mean velocity (A_{um}, red) are obtained along with the propagation direction. The vertical lines indicate the 4-day segments in Figures 16a–16c. NIW (b) horizontal wavelength, (c) phase, and (d) potential energy density (E_p) are obtained from complex means of the amplitude fits in 3 depth ranges (black lines are from 60 to 179 m, light blue lines are 60–119 m, and blue lines are 120–179 m for quantities derived from σ_θ; red lines are from $\boldsymbol{u_m}$). (e) Kinetic energy density is assessed as both E_{km} and $E_{k\sigma}$ from the directional fits to u_m and σ_θ at $\omega = 1.1f$, while two additional frequencies highlight this sensitivity. (f) Total energy density (E) is the sum of E_p (blue line, Figure 17d) and either E_{km} or $E_{k\sigma}$ at $1.1f$ (red or blue lines; Figure 17e). E from float 8653 (dashed lines; dotted lines subject to edge effects) is also plotted from the sum of E_p and $E_{k\sigma}$ at $1.1f$ (blue and red lines, Figure 12a). $F_z = c_{gz}E$ and for simplicity the right hand axis is simply a scaling by a constant $c_{gz} = 107$ m day^{-1} (Table 2). NIW, near-inertial internal waves.

The mean and standard deviation are 736 ± 187 km from 13 to 21 September. The initial length scale of 1,000 km for NIWs under Super Typhoon Mangkhut is estimated from the translation speed (6 m s^{-1}) over T_i. Another estimate of 700–800 km comes from the diameter of tropical storm winds (18 m s^{-1} from 13 to 14September) as the TC passed over the floats (light gray circle, Figures 1a and 1b). Directional fits of $\boldsymbol{u_m}$ and σ_θ from 120–179 m at the most energetic times (September 13–16) show λ_h closer to 500 km (red and blue lines, Figure 17b), after which A_{um} and λ_h decrease substantially. This difference between λ_h from $\boldsymbol{u_m}$ and σ_θ likely arises from using a depth-mean measurement (i.e., $\boldsymbol{u_m}$) to observe NIWs with large m.

We compare our various calculations of depth-mean E_k. Given ω, we convert E_p (blue line at $\omega = 1.1f$; Figure 17d) to $E_{k\sigma}$ via the polarization relations (blue line at $\omega = 1.1f$ and shading over the range 1.06–1.20f; Figure 17e; Equation 15). Similar directional fits are made for $\boldsymbol{u_m}$, with E_{km} about half of the value of $E_{k\sigma}$ (red vs. blue line; Figure 17e) and similarly for E and F_z (Figure 17f). The relevant limits appear to be $\omega = 1.10$–$1.25f$, which are based on the scalograms and comparisons of depth-mean u_σ and u_m (Figures 7 and 11) and the overlap of E_{km} and $E_{k\sigma}$ at $1.10f$ (red line and shading in Figure 17e). Lastly in Figure 17f, good comparison is noted for E and F_z from the directional fits to the float array data (solid lines) with that from the single closest float (dashed lines). Our values of E_k range from 40–100 J m^{-3} (Figure 17e). Substantial variability of background ocean conditions (e.g., mesoscale eddies) and TC properties (e.g., translation speed) contribute to wide-ranging values of E_k: 50 J m^{-3} under category-1 TCs and 20–200 J m^{-3} under category-5 TCs (Brooks, 1983; Jaimes & Shay, 2010; Nilsson, 1995; Pallàs-Sanz et al., 2016; Price, 1983).

The downward energy flux is: $F_{zm} = c_{gz}E_m$ and similarly for $F_{z\sigma}$. Maximum $F_{zm}/F_{z\sigma}$ is 0.05/0.08 W m^{-2} (Figure 17f), which is calculated using the maximum $c_{gz} = 107$ m day^{-1} for $\omega = 1.1f$ and $\lambda_h = 1{,}000$ km (Table 2). For $\lambda_h = 500$–$1{,}000$ km and depending on $\partial_z u$, c_{gz} varies from 53–145 m day^{-1} or about 50%, which yields a range of plausible values for maximum $F_{zm} = 0.02$–0.07 W m^{-2} and $F_{z\sigma} = 0.04$–0.11 W m^{-2}. These estimates are comparable to previous estimates of 0.01–0.08 W m^{-2} (Brooks, 1983; Jaimes & Shay, 2010; Pallàs-Sanz et al., 2016). The larger values are noted amidst a vigorous mesoscale eddy field in the Gulf of Mexico. Previous observations show F_z is about 2% of P or about 10% of P' (Cuypers et al., 2013; Pallàs-Sanz et al., 2016). However, a range of uncertainty from 2% to 33% of P' is noted (Cuypers et al., 2013). Our model's $\langle P \rangle$ and $\langle P' \rangle$ on 13 September are 3.0 W m^{-2} and 1.3 W m^{-2}. So our measured $F_{z\sigma}$ is 1%–4% of the modeled $\langle P \rangle$ and 3%–8% of $\langle P' \rangle$. In our observations, c_{gz} and thereby F_z are elevated because: (a) ω reaches 1.10–1.25f due to the wake's mesoscale relative vorticity and (b) shear is large in the wake and the NEC. The wide range of our values is due to the plausible ranges of λ_h and ω. The latter affects our calculations of $E_{k\sigma}$ from E_p because of the sensitivity of their ratio near f (Equation 13).

Similar directional fits are used to identify the interfacial wave with $\lambda_h \approx 65$–108 km (Figure 14 and Section 7). Wave amplitudes of σ_θ are obtained from harmonic fits to all 4 floats at $\omega = 1.1f$ for varying wavenumbers from 17 to 21 September (Figure 18). Resolution of λ_h is improved to 10 km. Fit amplitudes are squared and scaled to form E_p, which is averaged from 50 to 99 m, covering the largest amplitudes of the interfacial wave (Figure 14). Maximum amplitude is found for westward propagation at $\lambda_h = 75$ km (black vector, Figure 18), with a wide arc of energy from southwestward to north-northwestward within $\lambda_h \approx 50$–100 km. In summary, the interfacial wave propagates westward with $\lambda_h = 75$ km, in agreement with other assessments in Section 7.

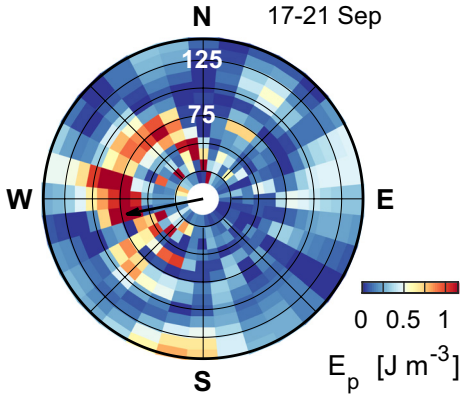

Figure 18. To identify the interfacial wave (Figure 14 and Section 7), wave amplitudes of potential density from 17 to 21 September are obtained from harmonic fits to all 4 floats at $\omega = 1.1f$ for varying wavenumbers and averaged over 50–99 m (but with better resolution of $\boldsymbol{k}$ compared to Figure 16b). These amplitudes are then scaled, squared, and plotted as potential energy. Broad westward propagation at $\lambda_h \approx$ 50–100 km is shown and the maximum amplitude is at 75 km (black vector). Float locations are in Figure 16d (gray or black lines).

9. Summary

With a sufficiently large array of rapidly-profiling floats during TC passage, NIW forcing and related changes in oceanic heat content have been studied by intentional and fortuitous placement of assets (D'Asaro et al., 2007; Jayne & Bogue, 2017; Johnston et al., 2020; Mrvaljevic et al., 2013; Sanford et al., 2011). Our float array drifted in Super Typhoon Mangkhut's wake, which affected NIW propagation. By measuring surface and depth-mean velocities as well as density profiles, the float array observed southward NIW propagation in the TC wake. Since NIWs have flat aspect ratios, their vertical propagation is slow (Alford et al., 2016). It is well known that mesoscale eddies alter the vertical propagation of NI energy into the interior (Kunze, 1985) and specifically under a TC (Jaimes & Shay, 2010; Pallàs-Sanz et al., 2016). Here, the persistent and broad coverage in time and space of the float array shows the wake itself is a source of mesoscale shear and vorticity. The effective vorticity and NI frequency reaches 1.1–1.25f. The background shear in the mesoscale TC wake and the NEC further enhance vertical energy propagation (i.e., the vertical group velocity, c_{gz}) on the cyclonic southern edge of the wake. This impact of a mesoscale TC wake matters because it offers a route for enhanced NI energy propagation into the interior. The exponential decay scale of mixed layer energy is 2.7 and 2.9 days at the 2 closest floats.

Since we lacked in situ atmospheric measurements as well as currents on the right side of the TC, the energy flux from the winds to mixed layer currents is calculated with a high-resolution model of this TC: total $\langle P \rangle = 3.0$ W m^{-2}. The NI component is: $\langle P' \rangle = 1.3$ W m^{-2}. The downward energy flux is: $F_z = c_{gz}E = c_{gz}(E_{k\sigma} + E_p) = 0.04$–$0.11$ W m^{-2} based only on the measurement of depth-dependent σ_θ. E_p is converted to $E_{k\sigma}$ (which denotes E_k calculated from σ_θ) based on the polarization relations for internal waves. The fraction of total power input, which ends up in NIW is $F_z/\langle P \rangle = 1\%$–$4\%$ and similarly for NI power input: $F_z/\langle P' \rangle = 3\%$–$8\%$. The float observations were under the TC and to its left with less coverage on the right side. However, we expect larger NIWs on the right side (Price, 1983). We speculate, that a larger $F_z/\langle P' \rangle$ ratio would have been measured on the right side, which previous measurements indicate is about 10%, but a wide uncertainty is also noted from 2% to 33% (Cuypers et al., 2013; Pallàs-Sanz et al., 2016). Numerical simulations show $F_z/P' \sim 10\%$–30% (von Storch et al., 2007; Furuichi et al., 2008; Zhai et al., 2009). Due to the limited profiling depth, F_z from perturbation pressure-velocity correlations cannot be calculated (Cuypers et al., 2013). Since (a) NI E_k is about an order of magnitude larger than E_p and (b) their ratio depends strongly on frequency near f, there is at least a 50% uncertainty solely based on the observed variability of frequency from a wavelet analysis. Furthermore, c_{gz} was not directly measured, but obtained from the dispersion relation. For a given frequency, c_{gz} varies by about 50% depending on mesoscale shear and NI horizontal wavelength. Due to the spatial coverage of the float array, we are able to assess the decreasing wavelength over time by using the array as a NIW antenna (Johnston et al., 2015), which is itself a novel method and result.

This antenna was also useful in detecting a westward propagating interfacial or mode-2 wave in the strongly-stratified transition layer, which lies between the mixed layer and interior. A mode-2 wave displaces shallower/deeper isopycnals up-/downwards. This NIW propagates in the westward NEC, which has a similar magnitude to the NI currents. As the NIW currents oppose/reinforce the mean flow, convergences/divergences arise. Isopycnals are strained in a manner consistent with a mode-2 wave. In the mean flow of the NEC, the isopycnal displacements act as topography and lead to the generation of shorter, secondary NIWs, which propagate down-/upwards into the interior/mixed layer. The exponential decay scale for this energy was 5.0 days at the closest float, but the passage of another TC complicates matters. Similar flow over transition layer obstacles is noted for near-N waves and NIWs (Bell, 1978; Czeschel & Eden, 2019; Polton et al., 2008). Such pre-existing upward-propagating NIWs affect subsequent wind work on the ocean (Plueddemann & Farrar, 2006). Also, the mode-2 wave has velocities and displacements, which are out of

phase across the transition layer and augment shear and strain, which in turn may lead to further mixing in the wake.

Data Availability Statement

Float data are available at the PISTON data site at https://www-air.larc.nasa.gov/cgi-bin/ArcView/camp2ex?TRAJECTORY=1#JOHNSTON.SHAUN/. Model results are available at https://doi.org/10.5281/zenodo.4134671. SST data were downloaded from the Asia-Pacific Data-Research Center at http://apdrc.soest.hawaii.edu/. Typhoon best track data were downloaded from the Joint Typhoon Warning Center at https://www.metoc.navy.mil/jtwc/products/best-tracks/2018/2018s-bwp/bwp2018.zip. We thank three anonymous reviewers for their helpful comments.

Acknowledgments
This work is supported by grant NA17OAR4310259 (TMSJ, DLR) from the Climate Variability and Predictability program at NOAA and N00014163085 (JNM) and N000141613073 (CYL, AS, SW) from the Office of Naval Research's PISTON initiative, which are components of the international Years of the Maritime Continent program. We are grateful to the master, crew, and science party on R/V Thomas Thompson for their help in deploying the floats. The Instrument Development Group at the Scripps Institution of Oceanography designed, prepared, and monitored the SOLO-II floats.

References

Alford, M. H., MacKinnon, J. A., Simmons, H. L., & Nash, J. D. (2016). Near-inertial internal gravity waves in the ocean. *Annual Review of Marine Science*, *8*(1), 95–123. https://doi.org/10.1146/annurev-marine-010814-015746

Bell, T. H. (1975). Topographically generated internal waves in the open ocean. *Journal of Geophysical Research*, *80*(3), 320–327. https://doi.org/10.1029/JC080i003p00320

Bell, T. H. (1978). Radiation damping of inertial oscillations in the upper ocean. *Journal of Fluid Mechanics*, *88*(2), 289–308. https://doi.org/10.1017/S0022112078002116

Brooks, D. A. (1983). The wake of Hurricane Allen in the western Gulf of Mexico. *Journal of Physical Oceanography*, *13*, 117–129. https://doi.org/10.1175/1520-0485(1983)013⟨0117:TWOHAI⟩2.0.CO;2

Chang, S. W., & Anthes, R. A. (1978). Numerical simulations of the ocean's nonlinear, baroclinic response to translating hurricanes. *Journal of Physical Oceanography*, *8*(3), 468–480. https://doi.org/10.1175/1520-0485(1978)008⟨0468:NSOTON⟩2.0.CO;2

Chen, S. S., & Curcic, M. (2016). Ocean surface waves in Hurricane Ike (2008) and Superstorm Sandy (2012): Coupled model predictions and observations. *Ocean Modelling*, *103*, 161–176. https://doi.org/10.1016/j.ocemod.2015.08.005

Chu, J.-H., Sampson, C. R., Levine, A. S., & Fukada, E. (2002). *The Joint typhoon warning center tropical cyclone best-tracks, 1945–2000* Tech. Rep. No. NRL/MR/7540-02-16). Joint Typhoon Warning Center.

Curcic, M., Chen, S. S., & Özgökmen, T. M. (2016). Hurricane-induced ocean waves and Stokes drift and their impacts on surface transport and dispersion in the Gulf of Mexico. *Geophysical Research Letters*, *43*(6), 2773–2781. https://doi.org/10.1002/2015GL067619

Cuypers, Y., Le Vaillant, X., Bouruet-Aubertot, P., Vialard, J., & McPhaden, M. J. (2013). Tropical storm-induced near-inertial internal waves during the Cirene experiment: Energy fluxes and impact on vertical mixing. *Journal of Geophysical Research: Oceans*, *118*(1), 358–380. https://doi.org/10.1029/2012JC007881

Czeschel, L., & Eden, C. (2019). Internal wave radiation through surface mixed layer turbulence. *Journal of Physical Oceanography*, *49*(7), 1827–1844. https://doi.org/10.1175/JPO-D-18-0214.1

Davis, R. E., Sherman, J. T., & Dufour, J. (2001). Profiling ALACEs and other advances in autonomous subsurface floats. *Journal of Atmospheric and Oceanic Technology*, *18*(6), 982–993. https://doi.org/10.1175/1520-0426(2001)018⟨0982:PAAOAI⟩2.0.CO;2

Davis, C., Wang, W., Chen, S. S., Chen, Y., Corbosiero, K., DeMaria, M., & Xiao, Q. (2008). Prediction of landfalling hurricanes with the Advanced Hurricane WRF Model. *Monthly Weather Review*, *136*(6), 1990–2005. https://doi.org/10.1175/2007MWR2085.1

Donlon, C., Robinson, I., Casey, K. S., Vazquez-Cuervo, J., Armstrong, E., Arino, O., & Rayner, N. (2007). The global ccean data assimilation experiment high-resolution Sea surface temperature Pilot project. *Bulletin of the American Meteorological Society*, *88*(8), 1197–1214. https://doi.org/10.1175/BAMS-88-8-1197

D'Asaro, E. A., Black, P. G., Centurioni, L. R., Chang, Y.-T., Chen, S. S., Foster, R. C., & Wu, C.-C. (2014). Impact of typhoons on the ocean in the Pacific. *Bulletin of the American Meteorological Society*, *95*(9), 405–418. https://doi.org/10.1175/BAMS-D-12-00104.1

D'Asaro, E. A., Eriksen, C. C., Levine, M. D., Niiler, P., Paulson, C. A., & Meurs, P. V. (1995). Upper ocean inertial currents forced by a strong storm, Part I: Data and comparisons with linear theory. *Journal of Physical Oceanography*, *25*, 2909–2936.

D'Asaro, E. A., Sanford, T. B., Niiler, P. P., & Terrill, E. J. (2007). Cold wake of Hurricane Frances. *Geophysical Research Letters*, *34*. https://doi.org/10.1029/2007GL030160

Furuichi, N., Hibiya, T., & Niwa, Y. (2008). Model-predicted distribution of wind-induced internal wave energy in the world's oceans. *Journal of Geophysical Research*, *113*. https://doi.org/10.1029/2008JC004768

Gill, A. E. (1982). *Atmosphere-Ocean dynamics*. Academic Press.

Hersbach, H., Bell, B., Berrisford, P., Hirahara, S., Horányi, A., Muñoz-Sabater, J., & Thépaut, J.-N. (2020). The ERA5 global reanalysis. *Quarterly Journal of the Royal Meteorological Society*, *146*(730), 1999–2049. https://doi.org/10.1002/qj.3803

Hong, S.-Y., Noh, Y., & Dudhia, J. (2006). A new vertical diffusion package with an explicit treatment of entrainment processes. *Monthly Weather Review*, *134*(9), 2318–2341. https://doi.org/10.1175/MWR3199.1

Iacono, M. J., Delamere, J. S., Mlawer, E. J., Shephard, M. W., Clough, S. A., & Collins, W. D. (2008). Radiative forcing by long-lived greenhouse gases: Calculations with the AER radiative transfer models. *Journal of Geophysical Research–D: Atmospheres*, *113*(D13). https://doi.org/10.1029/2008JD009944

Jaimes, B., & Shay, L. K. (2010). Near-inertial wave wake of Hurricanes Katrina and Rita over mesoscale oceanic eddies. *Journal of Physical Oceanography*, *40*(6), 1320–1337. https://doi.org/10.1175/2010JPO4309.1

Jayne, S., & Bogue, N. (2017). Air-deployable profiling floats. *Oceanography*, *30*(2), 29–31. https://doi.org/10.5670/oceanog.2017.214

Johnston, T. M. S., Chaudhuri, D., Mathur, M., Rudnick, D., Sengupta, D., Simmons, H., & Venkatesan, R. (2016). Decay mechanisms of near-inertial mixed layer oscillations in the Bay of Bengal. *Oceanography*, *29*(2), 180–191. https://doi.org/10.5670/oceanog.2016.50

Johnston, T. M. S., & Rudnick, D. L. (2009). Observations of the transition layer. *Journal of Physical Oceanography*, *39*, 780–797.

Johnston, T. M. S., Rudnick, D. L., Brizuela, N., & Moum, J. N. (2020). Advection by the North Equatorial Current of a cold wake due to multiple typhoons in the western Pacific: Measurements from a profiling float array. *Journal of Geophysical Research: Oceans*, *125*. https://doi.org/10.1029/2019JC015534

Johnston, T. M. S., Rudnick, D. L., & Kelly, S. M. (2015). Standing internal tides in the Tasman Sea observed by gliders. *Journal of Physical Oceanography*, *45*, 2715–2737. https://doi.org/10.1175/JPO-D-15-0038.1

Kumar, P., & Foufoula-Georgiou, E. (1997). Wavelet analysis for geophysical applications. *Reviews of Geophysics*, *35*(4), 385–412. https://doi.org/10.1029/97RG00427

Kunze, E. (1985). Near-inertial wave propagation in geostrophic shear. *Journal of Physical Oceanography*, *15*, 544–565.

Leaman, K. D., & Sanford, T. B. (1975). Vertical energy propagation of inertial waves: A vector spectral analysis. *Journal of Geophysical Research*, *80*(15), 1975–1978.

Morrison, H., Thompson, G., & Tatarskii, V. (2009). Impact of cloud microphysics on the development of trailing stratiform precipitation in a simulated squall line: Comparison of one- and two-moment schemes. *Monthly Weather Review*, *137*(3), 991–1007. https://doi.org/10.1175/2008MWR2556.1

Mrvaljevic, R. K., Black, P. G., Centurioni, L. R., Chang, Y.-T., D'Asaro, E. A., Jayne, S. R., & Sanford, T. B. (2013). Observations of the cold wake of Typhoon Fanapi (2010). *Geophysical Research Letters*, *40*, 316–321. https://doi.org/10.1029/2012GL054282

Nilsson, J. (1995). Energy flux from traveling hurricanes to the oceanic internal wave field. *Journal of Physical Oceanography*, *25*, 558–573. https://doi.org/10.1175/1520-0485(1995)025⟨0558:EFFTHT⟩2.0.CO;2

Niu, G.-Y., Yang, Z.-L., Mitchell, K. E., Chen, F., Ek, M. B., Barlage, M., & Xia, Y. (2011). The community Noah land surface model with multiparameterization options (Noah-MP): 1. Model description and evaluation with local-scale measurements. *Journal of Geophysical Research*, *116*(D12). https://doi.org/10.1029/2010JD015139

Pallàs-Sanz, E., Candela, J., Sheinbaum, J., & Ochoa, J. (2016). Mooring observations of the near-inertial wave wake of Hurricane Ida (2009). *Dynamics of Atmospheres and Oceans*, *76*, 325–344. https://doi.org/10.1016/j.dynatmoce.2016.05.003

Plueddemann, A. J., & Farrar, J. T. (2006). Observations and models of the energy flux to mixed-layer inertial currents. *Deep-Sea Research II*, *53*, 5–30.

Pollard, R. T., & Millard, R. C. (1970). Comparison between observed and simulated wind-generated inertial oscillations. *Deep-Sea Research*, *17*, 153–175. https://doi.org/10.1016/0011-7471(70)90043-4

Polton, J. A., Smith, J. A., MacKinnon, J. A., & Tejada-Martinez, A. E. (2008). Rapid generation of high-frequency internal waves beneath a wind and wave forced oceanic surface mixed layer. *Geophysical Research Letters*, *35*, L13602. https://doi.org/10.1029/2008GL033856

Price, J. F. (1981). Upper ocean response to a hurricane. *Journal of Physical Oceanography*, *11*, 153–175.

Price, J. F. (1983). Internal wave wake of a moving storm. Part I: Scales, energy budget and observations. *Journal of Physical Oceanography*, *13*(4), 949–965.

Sanford, T. B., Price, J. F., & Girton, J. B. (2011). Upper-ocean response to Hurricane Frances (2004) observed by profiling EM-APEX floats. *Journal of Physical Oceanography*, *41*, 1041–1056. https://doi.org/10.1175/2010JPO4313.1

Schönau, M. C., & Rudnick, D. L. (2015). Glider observations of the North Equatorial Current in the western tropical Pacific. *Journal of Geophysical Research: Oceans*, *120*, 3586–3605. https://doi.org/10.1002/2014JC010595

Skamarock, W. C., Klemp, J. B., Dudhia, J., Gill, D. O., Barker, D. M., Duda, M. G., & Powers, J. G. (2008). *A description of the advanced Research WRF version 3. NCAR tech. Note NCAR/TN-475+STR (tech. Rep.)*, Boulder, CO: National Center for atmospheric Research. https://doi.org/10.5065/D68S4MVH

Torrence, C., & Compo, G. P. (1998). A practical guide to wavelet analysis. *Bulletin of the American Meteorological Society*, *79*(1), 61–78.

von Storch, J.-S., Sasaki, H., & Marotzke, J. (2007). Wind-generated power input to the deep ocean: An estimate using a 1/10° general circulation model. *Journal of Physical Oceanography*, *37*(3), 657–672. https://doi.org/10.1175/JPO3001.1

Wallcraft, A. J., Metzger, E. J., & Carroll, S. N. (2009). Software design description for the HYbrid Coordinate Ocean Model (HYCOM) version 2.2 Tech. Rep., NRL/MR/732009-9166 (Tech. Rep.). Naval Research Laboratory.

Young, W. R., & Ben Jelloul, M. (1997). Propagation of near-inertial oscillations through a geostrophic flow. *Journal of Marine Research*, *55*, 735–766. https://doi.org/10.1357/0022240973224283

Zhai, X., Greatbatch, R. J., Eden, C., & Hibiya, T. (2009). On the loss of wind-induced near-inertial energy to turbulent mixing in the upper ocean. *Journal of Physical Oceanography*, *39*(11), 3040–3045. https://doi.org/10.1175/2009JPO4259.1

Zhao, Z., Alford, M. H., Simmons, H. L., Brazhnikov, D., & Pinkel, R. (2018). Satellite investigation of the M2 internal tide in the Tasman Sea. *Journal of Physical Oceanography*, *48*(3), 687–703. https://doi.org/10.1175/JPO-D-17-0047.1